A New Femtosecond Laser-Based 3D Tomography Technique

by

McLean P. Echlin

A dissertation submitted in partial fulfillment
of the requirements for the degree of
Doctor of Philosophy
(Materials Science and Engineering)
in The University of Michigan
2011

Doctoral Committee:

Professor Tresa M. Pollock, Co-Chair
Professor J. Wayne Jones, Co-Chair
Professor Steve M. Yalisove
Assistant Professor Samantha H. Daly

For my parents and educators

ACKNOWLEDGEMENTS

Many thanks to all the past and present group members, scientists, and collaborators for continuing to make this experience so enjoyable on a daily basis. I would also like to thank my committee members for their efforts, specifically T.M. Pollock for giving me the opportunity to be here.

TABLE OF CONTENTS

DEDICATION ii

ACKNOWLEDGEMENTS iii

LIST OF FIGURES vii

LIST OF TABLES xviii

LIST OF APPENDICES xix

ABSTRACT xx

CHAPTER

I. Introduction 1

1.1 Motivation for 3D 2
1.2 Tomography 4
1.3 Femtosecond Laser Based Tomographic Technique 5
1.4 Computational Power and Data Storage 6

II. Background 8

2.1 Existing Tomographic Techniques 9
2.1.1 Dual Beam FIB 9
2.1.2 X-Ray Tomography 11
2.1.3 Mechanical Serial Sectioning 13
2.1.4 Current Challenges with 3D Tomographic Techniques 15
2.2 UHS Steel 15
2.2.1 Applications and Background 16
2.2.2 Microstructure and Chemistry 17
2.2.3 Mechanical Properties 24
2.2.4 Failure Modes 24
2.3 Femtosecond Lasers 29
2.3.1 Laser Characteristics 29

2.3.2 Ablation/Energy Transfer 32
2.3.3 Femtosecond Laser Machining 35
2.3.4 Damage Thresholds 36

III. Laser-Material Interactions 39

3.1 Single Pulse Laser Studies 39
3.1.1 Morphological Characterization 44
3.1.2 Single Pulse Ablation Rate 45
3.2 Single Pulse Characterization of 4330 Steel & TiN 46
3.3 Bulk Material Removal 53

IV. The Femtosecond Laser Based Serial Sectioning Technique . 55

4.1 FSLSS Components 56
4.2 Layer-by-Layer Material Removal 60
4.3 Material Removal Rates 62
4.3.1 Profilometry 62
4.3.2 Autofocus Depth Profiling 64
4.4 Image Acquisition 65
4.5 Image Segmentation Routines 66
4.6 Reconstruction Methods 67
4.7 Ablation Artifacts 68

V. Fracture Toughness and 3D Characterization of 4330 Steel . 74

5.1 Precipitates in Steel 74
5.2 Structure Property Modeling 76
5.2.1 Void Nucleation Models 78
5.2.2 Void Growth Models 81
5.2.3 Other Particle Parameters 83
5.2.4 Cohesion Models 86
5.2.5 Finite Element Analysis 88
5.2.6 Multiscale Modeling with Homogenized Constitutive Relations 89
5.3 FSLSS of 4330 Steel 94
5.4 Single Pulse Femtosecond Laser Ablation 94
5.4.1 Single Pulse Ablation of TiN and 4330 Steel 96
5.5 TiN Particles Reconstructed in 4330 Matrix 97
5.6 Characterization of Inclusions 100
5.7 Comparison of 2D and 3D TiN Statistics 101
5.7.1 Validation - Particle Shapes and Sizes 102
5.7.2 Stereology 103
5.8 Comparison to Mechanical Serially Sectioned Datasets 106
5.9 Modeling of Toughness in 4330 Steel 108

5.9.1 Plastic Zone . . . 109
5.9.2 Representative Volume Elements . . . 113
5.9.3 FSLSS Modeling Analysis . . . 115
5.10 Multimodal Data Collection . . . 126

VI. TriBeam System - High Resolution, Multimodal FSLSS . . . 129

6.1 Tri-Beam System . . . 129
6.2 Hardware Components . . . 130
6.2.1 DualBeam FIB/SEM . . . 131
6.2.2 Femtosecond Laser . . . 131
6.2.3 Optical Setup . . . 132
6.2.4 Optical feed-through port . . . 133
6.2.5 Micro-Stage . . . 134
6.2.6 Energy Dispersive Spectroscopy Detector - EDS . . . 137
6.2.7 Electron Backscatter Diffraction Detector - EBSD . . . 137
6.3 Calibration and Integration . . . 137
6.3.1 Stage Control . . . 138
6.3.2 Laser Beam Alignment . . . 139
6.3.3 Beam Control . . . 140
6.3.4 Ablation Parameters . . . 140
6.4 Preliminary Data . . . 141

VII. Summary, Conclusions & Future Work . . . 145

7.1 FSLSS . . . 145
7.2 Toughness Modeling of a 4330 Steel . . . 148
7.3 The TriBeam System . . . 150
7.4 Future Work . . . 151
7.4.1 Layered Metallic/Ceramics . . . 152
7.4.2 Co-Al-W Alloy . . . 155
7.4.3 Accumulative Roll Bonded Cu-Nb Nanolaminates . . . 156
7.4.4 Polycrystalline Titanium . . . 158
7.4.5 Semiconductor Device Decomposition and Characterization . . . 159

APPENDICES . . . 160

BIBLIOGRAPHY . . . 188

LIST OF FIGURES

Figure

2.1 Dual-beam FIB stage views (a & c) showing the numerous detectors in proximity of the sample. Schematic sample positions (b & d) during milling and electron backscatter detection EBSD. (Image from G.D. West [44]). 11

2.2 (left) Schematic of X-ray tomography setup in which the sample is rotated between the source and the detector. (right) The voxel resolution of the technique is dependent upon the (1) magnification that is determined by the geometric ratio of the focus to object distance (FOD) to the focus to detector distance (FOD), (2) the detector resolution, and (3) the focal spot size of the X-ray source. (Image from O. Brunke [46]). 12

2.3 Synchrotron X-ray image of Ni-Al dendritic structure. Elemental segregation is shown by false color derived from the varied absorption contrast of the regions. (Image compliment of N. Husseini [54]). . . 13

2.4 3D reconstruction of Ti-21s. (a) 4380 β grains collected with an entire reconstructed volume of $1115 \times 516 \times 300\,\mu m$ (b) Individual reconstructed β grains of different sizes with the corresponding number of faces annotated [58]. 15

2.5 A 4340 plate steel after ballistic impact with visible shear localization that is visible in the form of white bands [17]. (Image from J.G. Cowie et al [17]) 17

2.6 A TEM image showing prior austenite grain size (in solid white lines) and martensite packet laths (in dashed white lines) in a Fe-0.2C-1.5Mn-0.15V steel with grain size of 2.3 µm. (Image from S. Morito [66]) 19

2.8 An optical micrograph showing the lath martensite structure for a low-temperature (200 hr at 400^o C) heat treatment. Martensite is present without any visible carbides or cementite. Image from R.N. Caron [68]. 19

2.7 A schematic showing the formation of carbides during the tempering process in martensitic steels and their corresponding carbon concentration profiles. Image from C. Brooks [67]. 20

2.9 An optical micrograph of tempered martensite with carbides and cementite present near retained austenite grain boundaries. Image from B. Bramfitt [69]. 21
2.10 An optical micrograph of 4330 steel with cuboidal red-colored TiN particles and smaller round black TiC particles 22
2.11 A BSE micrograph of FIB milled 4330 steel with two cuboidal TiN particles and smaller round dark grey TiC particles. The martensite laths are visible in light contrast grey scales in the background. (Image from M.D. Uchic [45]). 23
2.12 Single crystal niobium tensile test specimen showing shear bands and extreme deformation in the gauge section. (Image from C.N. Reid [74]). 25
2.13 A schematic illustrating the ductile fracture process. In (a) a specimen is necking down in the gauge region with greater applied stress. In (b) voids begin to nucleate at the center of the necked region where hydrostatic stresses are the largest. In (c) void-linkup and crack formation occur spreading radially outward toward the edge of the gauge section. Crack propagation tends to follow a zig-zag pattern along paths of greatest shear stresses. In (d) cracks have spread, and therefore cross-sectional area has decreased to a point where high stresses form brittle-type crack propagation. In (e) typical fracture surfaces are illustrated. (Image from T.B. Cox [72]). 26
2.14 SEM image of AISI 4340 steel ductile fracture surface. Nucleating cementite particles are marked with arrows. (Image from T.B. Cox [72]. 27
2.15 Schematic of (a) Pulse stretcher - two opposed antiparallel diffraction gratings with a telescope positioned in between them. An incoming pulse is chirped across its wavelengths with red having a shorter path than blue wavelength. Schematic of (b) Pulse compressor - two parallel diffraction gratings in which the blue has a shorter optical length than red wavelength. Schematic of (c) Temporal ranges of pulse widths throughout the chirped pulse amplification (CPA) process. (Image from G. Mourou [24]). 31
2.16 Simple example of the laser gain bandwidth, a mode-locked cavity, and the corresponding laser output. 31
2.17 EBSD map of a cross-sectioned single femtosecond laser pulse in a CMSX-4 superalloy. Dislocation densities of 2.8×10^{10} per cm^3 have been estimated from the measured strain. (Image from A. Kumar [103]). 34
2.18 TEM images prepared from a foil of CMSX-4 superalloy that was subsequently laser machined with low-fluence laser pulses ($0.392\,J/cm^2$) [99]. Dislocations extend radially less than 1-2 µms and the $\gamma - \gamma'$ two phase microstructure is unperturbed. 35

2.19 Femtosecond laser hole drilling is shown to produce less residual damage and a smaller heat-affected-zone (HAZ) than longer pulse laser machining and continuous-wave (CW) lasers. Laser machined holes using 780 nm wavelength at (right) 10 picosecond pulsed laser, a (middle) 1 picosecond pulsed laser, and a (left) 150 femtosecond pulsed laser [116]. 36
2.20 Ablation depths plotted for a range of fluences in CMSX-4 superalloy. Corresponding low and high fluence single pulse laser craters are shown in the upper left and right. Material removal rate slope is low for the low fluence range compared to the high fluence range (Image from S. Ma [88]). 37
2.21 Femtosecond laser drilled hole with a high aspect ratio and then sectioned laterally [88]. The SEM image shows low amounts (less than $1-2\,\mu m$ of redeposited material are present on the sides of the sides and the shoulder of the hole. Laser machining was performed with the number of pulses indicated in the image, at a fluence of $12.9\,J/cm^2$. 38
3.1 SEM image of single pulse laser machined spots on an area of 4330 steel. 41
3.2 CCD image of a the femtosecond laser beam at focus after a 20cm plano-convex focal lens with Gaussian beam profile. The $(1/e^2)$ spot size is $39.05\,\mu m$. 42
3.3 (left) AFM scan of single laser pulse in 4330 steel with peak fluence $\phi = 2.1\,J/cm^2$. A depth of 40 nm is apparent from the line profile on (right). 2D and 3D information is extracted from AFM scans. . . . 45
3.4 Squared diameter of measurements collected from AFM measurements for a 4330 steel irradiated with single laser pulses. An ablation threshold of $0.40\,J/cm^2$ was extrapolated from the fit of the squared diameter data by pulse energy. The $(1/e^2)$ spot size was calculated from the fit to be $20.2\,\mu m$. The $(1/e^2$ spot size is used to determine the laser fluence at the sample surface. The threshold fluence provides a material dependent scale for how much damage is being done to the sample. 47
3.5 Squared diameter measurements collected from AFM measurements for a 4330 steel irradiated with single laser pulses. An ablation threshold of $0.41\,J/cm^2$ was extrapolated from the fit of the squared diameter data by pulse energy. The $(1/e^2)$ spot size was calculated from the fit to be $19.8\,\mu m$. The $(1/e^2$ spot size is used to determine the laser fluence at the sample surface. The threshold fluence provides a material dependent scale for how much damage is being done to the sample. 48

3.6 Squared diameter measurements collected using an SEM for a 4330 steel irradiated with single laser pulses. An ablation threshold of $0.047\,\mathrm{J/cm^2}$ was extrapolated from the fit of the squared diameter data by pulse energy. The $(1/e^2)$ spot size was calculated from the fit to be 47.6 µm. The $(1/e^2$ spot size is used to determine the laser fluence at the sample surface. The threshold fluence provides a material dependent scale for how much damage is being done to the sample. 49
3.7 Single pulse ablation depths (nm) for 4330 steel plotted against laser fluence (J/cm^2). Ablation depths measured using AFM. 50
3.8 Squared diameter measurements collected using an AFM for 4330 steel irradiated with single laser pulses. An ablation threshold of $0.27\,\mathrm{J/cm^2}$ was extrapolated from the fit of the squared diameter data by pulse energy. The $(1/e^2)$ spot size was calculated from the fit to be 18.6 µm. The $(1/e^2$ spot size is used to determine the laser fluence at the sample surface. The threshold fluence provides a material dependent scale for how much damage is being done to the sample. 51
3.9 Ablation removal rates for 316 stainless steel [119], silicon [100], magnesium oxide [122], poly-methyl-methacrylate [121], gold [123], alumina [122], and silver [123]. All studies were conducted with 100-500 fs. pulses and all curves exhibit a low and high fluence ablation regime with a distinct transition at which the material removal rate sharply increases. This plot shows that materials with multiple phases can be laser machined with simultaneous material removal when their ablation rates are equal. This is only important for multi-phase material ablation where the beam has normal incidence to the sample surface. 52
3.10 Field emission gun (FEG) SEM images of single pulse laser shots on a 4330 steel sample. (left) peak laser fluence ϕ=$13.5\,\mathrm{J/cm^2}$ (top right) ϕ=$9.6\,\mathrm{J/cm^2}$ (bottom right) ϕ=$5.3\,\mathrm{J/cm^2}$. 53
4.1 (left) Schematic of FSLSS technique. Imaging pathway consists of a microscopy and objective lens coupled to a CCD and images in standard atmosphere. The laser-machining pathway consists of power attenuators and focusing optics. A three-axis stage with the sample rigidly affixed translates the sample and performs the machining steps. An in-situ spectrometer monitors the luminous plasma to capture chemical information. (right) Photographs of schematically shown FSLSS setup. 57

4.2 Schematic of stage motion for femtosecond laser machining. Accelerations are performed while a fast acting shutter stops the laser pulses. At constant velocities the shutter is opened to laser machine the sample surface. Stage translation is alternated between the horizontal and vertical machining patterns shown overlaid above. The machining patterns are offset by half of the line scan spacing every other iteration to reduce periodic machining artifacts and lower the average surface roughness. 58
4.3 Material removal rate plotted against the maximum sectionable volume for mechanical, FIB, and femtosecond laser based serial sectioning techniques. 60
4.4 Schematic and plot of data collected using a profilometer to characterize the step height for repeated square area laser ablation scans. The step size is 37.5 µm which was removed over the aggregate of 580 laser passes or about 64.7 nm/pass. Pulse overlap was less than 20%. 63
4.5 SEM image of 4330 steel after 80 µm of material removal using the FSLSS technique. Sample surface has an average roughness (Ra) of 0.5 µm. 64
4.6 The material removal, as determined by an autofocusing routine, is linear throughout the entire sectioning experiment (41 hours). The sample surface is brought into focus using a Fast-Fourier-Transform algorithm to provide open loop feedback for small stage movements. The stage position, at focus, is recorded for every slice and then plotted to determine the material removal rate. 65
4.7 (left) Raw optical image from FSLSS process with TiN inclusion particles identified with arrows. (middle) Same image after background subtraction and a local threshold being applied to the highest R/G/B color intensity ratio areas. (right) Same image in final segmented form with a disk filter smoothing routine and deletion of single pixel point detections with no nearest neighbors (26 total) in any plane. 67
4.8 Raw optical FSLSS images expanded from a schematic 2D segmented image stack. The images are assembled with a spacing equal to the material removal rate calculated for the specific FSLSS experiment. 68
4.9 Secondary electron SEM image of 16 laser pulses at 0.54 J/cm^2 on a single-crystal nickel based superalloy CMSX-4 [88]. Small ripple formations are shown to form at a length scale similar to that of the laser radiation (780 nm). The ripples are oriented parallel to the polarization of the laser wavefront. (left) low magnification. (right) high magnification 69

4.10 (top left) Laser machining of lanthanum oxide containing steel. The laser ablation scan paths are visible from line spacing that was larger than 50 % overlap. (top right) Mounds formed from nonuniform ablation of second phase lanthanum oxide precipitates in steel. (bottom left) Laser scan lines are visible and lanthanum oxide phases that have been exposed by sectioning. (bottom right) A peak has formed presumably from non-matched ablation of two phases, again in a lanthanum oxide containing steel. 70
4.11 Secondary electron SEM image of polycrystalline nickel with periodic machining artifacts due to non-optimized line spacing. The width of the artifacts is 9.2 µm, which was approximately equal to the scan line spacing. 72
4.12 SEM image of polycrystalline nickel after 200 µm of material removal using the FSLSS technique in vacuum. Periodic structures have formed as a result of the 9.3 µm line spacing. 72
4.13 A schematic showing the line spacing, pulse spacing, and Gaussian beam profile. Periodic machining artifacts will occur if these parameters are not optimized. 73
5.1 3D block assembled schematically from optical micrographs imaged from three orthogonal surfaces of titanium modified 4330 steel. TiN inclusions appear red due to absorption contrast and are indicated with arrows. 76
5.2 Schematic of ductile fracture and the formation of voids at primary and secondary inclusion particles with increasing strain in a high strength steel [138]. In a 4330 steel, the smaller sized population of inclusions are sub-micron sized Ti(C,N) and the larger sized population of inclusions are 1-10 µm TiN particles. 78
5.3 Schematic showing the parameters influencing toughness modeling. Those marked with green dots are available from the FSLSS technique. The interfacial adhesion γ can be calculated using density functional theorgy (DFT) or interface strength measurements. . . . 91
5.4 Schematic of the length scales and microstructural interactions necessary for modeling ductile fracture [146]. A representative cracked sample is shown on the (left) with an inset r_K process zone where stress concentrations and triaxiality are enhanced due to the proximity to the crack tip. The damage region shows the relevant microstructure in a steel specimen, primary TiN particles with primary voids (l_1 sized), and secondary TiC particles with secondary voids (l_2 sized). 92
5.5 SEM image of 4330 steel after 80 slices of FSLSS machining for a cumulative removal depth of 45 µm. 96
5.6 Ablation depth per pulse for 316 stainless steel and a TiN coating. The ideal FSLSS machining range is below 2 J/cm^2. In this region the ablation rate for both materials is within 15 nm/pulse. All FSLSS experiments are performed in the fluence regime below 2 J/cm^2. . . 97

5.7 FSLSS reconstruction of TiN inclusions in 4330 titanium modified steel. 407 slice thick dataset with a 0.23 µm/slice sectioning resolution and an imaging resolution of 0.15 µm/pixel. (right) An individual TiN particle reconstructed showing the cuboidal nature of the particles and their large 8 µm diameters. 98
5.8 Linear material removal throughout the entire 41 hour dataset collection. Removal rate is measured using the calibrated three-axis high-precision stage coupled with the small depth of focus for the 20x objective microscope used to image the sample surface during a FSLSS experiment. 99
5.9 Various TiN particles deep etched out of the 4330 matrix. Their morphology is mostly cuboidal and they range in size from 1-10 µm. Some particles appear partially fractured or joined to other TiN particles. 103
5.10 (Top Image) Photostitched collection of optical micrograph of polished 4330 steel collected from a random 2D cross-section in the bar-end of a double-linear shear test specimen. Cuboidal titanium nitrides were segmented out from thunder-represente matrix using basic thresholding algorithms and gaussian filters to create a binary image (Bottom Image). 105
5.11 A 3D reconstruction of a mechanically serial sectioned dataset collected by S. Chan (Northwestern Univeristy) and D. Rowenhorst (NRL). The sample is taken from the process zone in a 4330 steel from an interrupted compact tension sample. The blue region is a crack propagated during the compact tension test and the yellow particles are TiN. A 4330 steel was analyzed with similar composition and processing conditions to the materials used in this thesis. The height of the plastic zone was estimated to be 112 µm, on average, while the extent of the plastic zone ahead of the crack was measured to be 73 µm. 108
5.12 Schematic showing the method of sampling using the FSLSS technique to analyze the titanium modified 4330 steel. Six FSLSS datasets are collected each having volume in the range of $\sim 10^8$ µm^3. Each of the six FSLSS datasets is sub-sampled into eight plastic zone sized regions having volumes on the order of $\sim 10^5$ µm^3. These 48 sub-sampled regions have then been used as a statistical volume elements (SVE) of different representative spatial distributions of TiN particles that exist in the original bulk 4330 steel specimen. This SVE has been used to calculated toughnesses of these distributions as they would exist provided a bulk sample had a distribution of particles similar to those found in the sub-sampled SVE region. 110
5.13 Variables available from the FSLSS technique that dictate the number of interacting particles in the plastic zone. The plastic zone size is calculated from material properties. Indicators of particles size, spacing, and density will define roughly how many interacting particles can fit within the plastic zone. 112

5.14 J_{IC} values predicted using the Olson-Wang toughness model (closed circles) plotted versus their relative cumulative density. A two-parameter Weibull fit is also shown (solid line). The mean J_{IC} value is 0.089 MPa(m), the median is 0.064 MPa(m). 118
5.15 J_{IC} values plotted against their relative probability densities according to the two-parameter Weibull fit. 119
5.16 Weibull plot of J_{IC} values and their relative probability of occurrence. A Weibull modulus, the slope or shape parameter, of the fit is 1.4 and the J_0 fitting value, or scale parameter, is 0.094 MPa(m). The variance of the data is indicated by the Weibull modulus and is in good agreement with toughness measurements made in bulk specimens by Ruggieri [188]. 120
5.17 K_{IC} values predicted using the toughness model (closed circles) plotted versus their relative cumulative density. A two-parameter Weibull fit for the cumulative density function is also shown (solid line). The mean K_{IC} value is 64.7 MPa($m^{1/2}$), the median is 59.4 MPa($m^{1/2}$). 121
5.18 K_{IC} values plotted against their relative probability densities according to the two-parameter Weibull fit. 122
5.19 Weibull plot of K_{IC} values and their relative probability of occurrence. A Weibull modulus, the slope or shape parameter, of the fit is 2.82 and the K_0 fitting value, or scale parameter, is 72.8 MPa($m^{1/2}$). The variance of the data is indicated by the Weibull modulus and is in close agreement with works by Ruggieri [188]. 123
5.20 Weibull plot of J_{IC} values and their relative probability of occurrence. 3D reconstructions of sub-sampled regions corresponding to the blue circled regions are shown relative to their toughness values. The minimum and average toughness values are important for modeling failure criteria in bulk structural material, suggesting that detailed toughness models for these sub-samples would help understand why these regions are limiting the overall toughness of the material. . . 124
5.21 Weibull plot of J_{IC} values and their relative probability of occurrence extracted from the Wang-Olson and Garrison-Moody models, as well as bulk ferritic C-Mn steel toughness data from Ruggieri [188]. Weibull modulus m values for the three datasets are respectively: 1.4 , 1.41 , and 1.4-1.5 126
5.22 Spectroscopic data for titanium modified 4330 steel and a TiN coating. Ionization states with high relative intensity for elements of pertinence are demarcated with arrows and labeled with their wavelength. 128
6.1 Schematic of the Tri-Beam system. 130
6.2 Schematic showing the laser interface port. The micrometers are used to translate and position the beam laterally. The depth of the microscope objective adapter tube can be adjusted externally to change the focal point inside the chamber. The translational and focal plane adjustments can be made while the system is under vacuum. . . . 134

6.3 Micropositioner stage rotated to (a.) 52° for FIB machining and imaging. (b.) Micropositioner stage rotated to -60° for femtosecond laser machining. (c.) Micropositioner stage rotated to 70° for EBSD data collection. (d.) Schematic showing the custom microstage components necessary for access to all detectors and beams within the DB-235 vacuum chamber. The EBSD detector is automatically extracted for all other imaging or machining steps. 135
6.4 Schematic showing the stage angles necessary for access to all detectors and beams within the DB-235 vacuum chamber. 136
6.5 Micropositioner stage schematic and rotator. 136
6.6 (left) Micropositioner stage rotated to 52° for FIB machining and imaging. (center) Micropositioner stage rotated to -59° for femtosecond laser machining. (right) Micropositioner stage rotated to 70° for EBSD data collection. 136
6.7 Femtosecond laser serial sectioning was performed with 5 or 15 passes of the standard ablation pattern, see Figure 4.2, at laser fluences of either $0.12\,J/cm^2$, $0.25\,J/cm^2$, or $0.37\,J/cm^2$. EBSD pattern were collected from all laser ablated regions, but with higher quality maps accessibly at lower fluences and lower numbers of passes. 141
6.8 SEM image of a laser machined area of polycrystalline nickel made using the femtosecond laser in the Tri-Beam system. Single laser pulses were deposited in succession to scribe the letter "U". Each 10 µm spot is a single laser pulse. 143
6.9 SEM image of a laser machined region of polycrystalline nickel and a smaller FIB machined area. Machining was done in vacuum. Laser machining required less than 60 seconds, while the FIB machining required 1.5 hours. 143
6.10 Using the Tri-Beam system, five slices were collected by laser machining polycrystalline nickel at a fluence of 1-4 J/cm^2. EBSD and secondary electron SEM images were collected for each slice. The sample was tilted, selectively machining part of the sample preferentially first. The EBSD imaging quality can be seen to decrease until the entire area is laser machined, at which point the surface quality reaches a steady state. By combining EBSD pattern collection with SEM imaging, segmentation of grains can be performed much more easily by comparing the boundaries in the two images. Furthermore, the EBSD information can be used to evaluate the effect of grain orientation texture, due to processing conditions, on mechanical properties. 144
7.1 Maximum addressable sample volumes and material removal rates plotted for FIB, mechanical, and femtosecond laser machining. . . 147

7.2 A schematic showing the five major failure mechanisms of thermal barrier coatings [197]. Datasets collected using the TriBeam system will identify the geometry of the interfaces between the layered systems and will characterize the porosity between the top coat, which allows the columns of ceramic to expand and contract upon thermal cycling without generating high residual stresses. 154
7.3 BSE images of TBC on a Rene N5 superalloy substrate with a Pt-aluminide bond coat after 100 thermal cycles to 1163°C (micrographs from R.W. Jackson [199]). 155
7.4 SEM micrograph showing a Co-base alloy heat treated at 900°C with μ and Co_3W phases. The μ phase has composition of 50W-47Co-2Al atomic%, the γ-γ'phase has composition 78Co-15W-9Al atomic%, and the Co_3W phase has composition 67Co-31W-2Al atomic% (micrographs from M. Titus [201]). 156
7.5 Optical micrograph of Cu-Nb nanolaminate material. Accumulative roll bonding is used to create thing layers of alternating Cu and Nb. (left) Elipsoidal Nb defects are visible between layers. (right) Intermixed elipsoidal Cu-Nb defects are present between layers. (micrographs from T. Nizolek [205]). 158
7.6 EBSD micrographs of Cu-Nb nanolaminate material. EBSD step size (micrographs from T. Nizolek [205]). 158
A.1 FSLSS dataset of size 404.4×301.7×82.9 µm, with imaging resolution of 0.16 µm/pixel and slice resolution of 0.56 µm/pixel. TiN volume fraction is 0.041 %, particle density is 3.6×10^{14} particles/m^3, mean particle size is 0.80 µm, and nearest neighbor spacing is 4.98 µm. . . 162
A.2 FSLSS dataset of size 404.4×301.7×77.9 µm, with imaging resolution of 0.16 µm/pixel and slice resolution of 0.56 µm/pixel. TiN volume fraction is 0.021 %, particle density is 1.1×10^{13} particles/m^3, mean particle size is 2.06 µm, and nearest neighbor spacing is 18.08 µm. . 163
A.3 FSLSS dataset of size 404.4×301.7×54.4 µm, with imaging resolution of 0.16 µm/pixel and slice resolution of 0.56 µm/pixel. TiN volume fraction is 0.019 %, particle density is 7.0×10^{12} particles/m^3, mean particle size is 2.78 µm, and nearest neighbor spacing is 25.17 µm. . 164
A.4 FSLSS dataset of size 404.4×301.7×149 µm, with imaging resolution of 0.17 µm/pixel and slice resolution of 0.43 µm/pixel. TiN volume fraction is 0.044 %, particle density is 2.0×10^{13} particles/m^3, mean particle size is 1.21 µm, and nearest neighbor spacing is 3.10 µm. . . 165
A.5 FSLSS dataset of size $314.1 \times 156.0 \times 89$ µm, with imaging resolution of 0.15 µm/pixel and slice resolution of 0.22 µm/pixel. TiN volume fraction is 0.028 %, particle density is 2.9×10^{13} particles/m^3, mean particle size is 2.12 µm, and nearest neighbor spacing is 9.97 µm. . . 166
A.6 FSLSS dataset of size $404.4 \times 301.7 \times 46$ µm, with imaging resolution of 0.16 µm/pixel and slice resolution of 0.50 µm/pixel. TiN volume fraction is 0.052 %, particle density is 1.9×10^{13} particles/m^3, mean particle size is 2.49 µm, and nearest neighbor spacing is 19.37 µm. . 167

A.7 FSLSS dataset of size $404.4 \times 301.7 \times 55\,\mu m$, with imaging resolution of $0.16\,\mu m$/pixel and slice resolution of $0.42\,\mu m$/pixel. TiN volume fraction is $0.029\,\%$, particle density is 1.4×10^{13} particles/m^3, mean particle size is $1.74\,\mu m$, and nearest neighbor spacing is $13.04\,\mu m$. . 168
C.1 Optical micrograph of laser machined magnesium sample with embedded alumina fibers before substantial ablation (left) and after ablation (right). Preferential ablation of the matrix is shown by the areas that are out of focus. The alumina fibers are exposed and are in focus. 186
C.2 Optical micrograph of laser machined magnesium sample with embedded alumina fibers before substantial ablation (left) and after ablation (right). Preferential ablation of the matrix is shown by the areas that are out of focus. The alumina fibers are exposed and are in focus. 187

LIST OF TABLES

Table

2.1 Composition in weight % of titanium modified 4330 steel. 23

5.1 FSLSS 3D dataset statistics of TiN inclusions in titanium modified 4330 steel. 100

5.2 Statistical comparison of an aggregated set of FSLSS datasets, 2D stereological collected particle information, and two mechanical serial sectioning datasets. Statistical analysis was performed using IDL code courtesy H. Jou (QUESTEK). 105

5.3 Table of size and statistical information related to datasets collected using the FSLSS technique. Smaller sample volumes (SVEs) were extracted from these datasets. 115

7.1 Comparison of various sectioning techniques: Atom Probe Tomography (APT), Focused Ion Beam Serial Sectioning (FIB-SS), Mechanical Serial Sectioning (Mech-SS), Femtosecond Laser Serial Sectioning (FSL-SS) 147

LIST OF APPENDICES

Appendix

A. FSLSS Dataset Reconstructions 161

B. Matlab Image Processing Segmentation Code 169

C. Femtosecond Laser Multipulse Machinining 186

ABSTRACT

A New Femtosecond Laser-Based 3D Tomography Technique

by

McLean P. Echlin

Co-Chairs: Tresa M. Pollock and J. Wayne Jones

Tomographic imaging has dramatically changed science, most notably in the fields of medicine and biology, by producing 3D views of structures which are too complex to understand in any other way. Current tomographic techniques require extensive time both for post-processing and data collection. Femtosecond laser based tomographic techniques have been developed in both standard atmosphere (femtosecond laser-based serial sectioning technique - FSLSS) and in vacuum (Tri-Beam System) for the fast collection ($10^5\,\mu m^3/s$) of mm^3 sized 3D datasets. Both techniques use femtosecond laser pulses to selectively remove layer-by-layer areas of material with low collateral damage and a negligible heat affected zone. To the authors knowledge, femtosecond lasers have never been used to serial section and these techniques have been entirely and uniquely developed by the author and his collaborators at the University of Michigan and University of California Santa Barbara.

The FSLSS was applied to measure the 3D distribution of TiN particles in a 4330 steel. Single pulse ablation morphologies and rates were measured and collected from literature. Simultaneous two-phase ablation of TiN and steel matrix was shown to occur at fluences of 0.9-2 J/cm^2. Laser scanning protocols were developed minimizing

surface roughness to 0.1-0.4 µm for laser-based sectioning.

The FSLSS technique was used to section and 3D reconstruct titanium nitride (TiN) containing 4330 steel. Statistical analysis of 3D TiN particle sizes, distribution parameters, and particle density were measured. A methodology was developed to use the 3D datasets to produce statistical volume elements (SVEs) for toughness modeling. Six FSLSS TiN datasets were sub-sampled into 48 SVEs for statistical analysis and toughness modeling using the Rice-Tracey and Garrison-Moody models. A two-parameter Weibull analysis was performed and variability in the toughness data agreed well with Ruggieri *et al.* bulk toughness measurements.

The Tri-Beam system combines the benefits of laser based material removal (speed, low-damage, automated) with detectors that collect chemical, structural, and topological information. Multi-modal sectioning information was collected after many laser scanning passes demonstrating the capability of the Tri-Beam system.

CHAPTER I

Introduction

Tomographic imaging has provided major scientific insights to problems in medicine, geology, oceanography, astronomy and materials science [1–5]. Two-dimensional (2D) slices that can be reconstructed into three-dimensional (3D) datasets are acquired with a wide variety of techniques that utilize electrons [6], neutrons [7], X-rays [8], ions [3, 9], visible light [1, 2], or acoustic waves [10]. The sectioning and imaging approach is constrained by the level of resolution required, physical size of the object being interrogated, nature of the interaction of the material(s) being imaged with the imaging probes, and destructive or non-destructive effects of the specific machining method. For multiphase engineering materials the availability of 3D information permits analysis of material features such as particle clustering [11, 12], spatial orientation and geometry [13], and phase interconnectivity [3], which are often misrepresented by 2D analysis of anisotropic materials [14]. For many materials, the rarely occurring features located at the tails of the size distribution govern properties such as fatigue life [15, 16] or shear strength [17, 18], and it is therefore critical to section large volumes of material to gain access to the microstructural statistics. For these reasons, application of existing tomographic techniques to multiphase materials (such as mechanical serial sectioning, FIB serial sectioning , and X-ray tomography), where phases with similar densities are intermixed at the µm-scale and dispersed

on the mm-scale, is particularly challenging because of maximum analyzable volume constraints (FIB serial sectioning and mechanical serial sectioning) and loss of imaging resolution with increased volume of analysis (X-ray tomography). In this thesis a new femtosecond laser-based tomographic imaging technique has been developed that addresses much larger material volumes compared to current techniques. Here the femtosecond laser serves as the primary material removal tool, permitting the direct ablation of material for the analysis of mm^3 to cm^3 volumes. A detailed summary of lasers, laser ablation, and existing tomographic techniques will be presented in Chapter II and Chapter III, along with an introduction to ductile fracture in steel, a topic later addressed with the laser technique. This rapid laser serial sectioning technique utilizes high repetition rate, ultrashort pulse femtosecond pulses for layer-by-layer material ablation that is applicable to a wide variety of materials. The femtosecond laser-based technique is discussed in detail in Chapter IV with comparisons to existing characterization techniques in Chapter V. Also in Chapter V, the distribution of titanium nitrides (TiN) in a 4330 steel is characterized using this new tomographic technique. The TiN precipitates in these steels are widely spaced and sized between 1-10 µm, and influence toughness in regions sized on the order of 100 µm in the vicinity of crack tips. The femtosecond laser based tomography technique has permitted the collection of samples from multiple regions in a sizable volume of material, both requirements necessary to model toughness in this steel system.

1.1 Motivation for 3D

Microstructural constituents in engineering materials are often assumed to be distributed homogeneously in 2D and 3D space. For systems where prior knowledge about the microstructure exists, 2D stereological methods can produce reasonable representations of the 3D features [19]. In systems with more complex microstructure and less prior knowledge about the microstructure, 3D data is essential for accu-

rate representations. Hung *et al* were able to determine the nucleation sites of grain boundary cementite, based on 3D reconstructions of pro-eutectoid cementite precipitates in a Fe-C-Mn steel alloy [20]. Characterization of the cementite precipitates by 3D serial sectioning revealed the precise location of cementite connectivity, strongly suggesting that cementite nucleates at austenite grain boundary edges and corners. Thornton and Poulsen simulated 2D and 3D microstructural coarsening of a binary 50/50% phase mixtures that had previously undergone spinodal decomposition. In the 2D case, as the phases coarsened, isolated regions (particles) form, whereas in 3D continuity is maintained for each phase. These models show that significantly different microstructures result from the added 2D to 3D dimensional effects [21]. For many processed materials with complex 3D structures such as directionally solidified superalloys, composites, forgings, and other wrought-processed alloys, there are often microstructural inhomogeneities that are indicative of material property anisotropies [22]. These materials tend to have complex morphology or topology that cannot be analyzed in 2D sections alone. The typical methods of 2D stereology [23] can misrepresent complex 3D features and may not sample heterogeneous microstructure properly. Additionally, 2D sections do not give the spatial distribution of phases, and also have a low statistical chance of capturing rarely occurring phases.

Ultra high strength steels are often precipitation strengthened via metallic additions such as titanium that form carbides such as $M_{23}C_6$ type or carbonitrides such as Ti(C,N). In a 4330 steel alloy investigated in this research, the addition of titanium can also result in the formation of deleterious TiN precipitates, which can significantly alter or degrade the fracture toughness, based on their spatial distribution. Heterogeneous distributions of the TiN inclusions will lead to increased material property anisotropy and spatial variability. Therefore, it would be advantageous to statistically characterize the arrangement, size, and spacing of the TiN precipitates. In the following section, requisite dataset sizes and resolution necessary to appropriately

characterize such metallurgical problems are considered.

1.2 Tomography

Tomography techniques either utilize penetrating radiation, such as x-rays or electrons, or a destructive serial sectioning process. Sectioning processes are applicable to a wide variety of material systems and may permit access to large volumes of material at higher nano-scale resolutions than x-ray tomography, especially in materials with similar elemental constituents and therefore poor absorption contrast. X-ray tomography techniques that rely on a point source for X-ray generation see a reduction in resolution with increased imaging volume. Numerous serial sectioning techniques presently exist, such as mechanical serial sectioning, focused ion beam (FIB) serial sectioning, and atom probe tomography, but there are still many challenges in acquiring specific types and volumes of 3D data.

Material properties are dependent on structural features that span a range of length scales. For most metals, strengthening arises from microstructural features that exist on the 100's of nm scale up to the 100's of µm. These features tend to be grains boundaries, precipitates, secondary phases, and voids. Precipitates and voids of µm scale can be distributed with spacings that are orders of magnitude higher, making 3D characterization difficult. In material systems (such as steels) where rarely occurring, small-volume-fraction precipitates dictate toughness, standard serial sectioning techniques are inadequately inefficient to capturing the volumes necessary to characterize the distribution of precipitates. The tomography technique developed here addresses the problem of characterizing submicron features that occur rarely, i.e., features that are present at small volume fractions.

1.3 Femtosecond Laser Based Tomographic Technique

In this thesis the development of a new 3D tomographic sectioning technique, referred to as femtosecond laser aided serial sectioning (FSLSS), is described. This technique utilizes a femtosecond laser to selectively section material with precisely controlled removal rates. Subsequently, 3D reconstruction are made from optically imaged microstructural data that has been image processed and segmented using our Matlab and IDL based code. Femtosecond laser pulses are particularly beneficial for machining material because they have high focused intensities ($> 10^{18}\,\mathrm{W/cm^2}$) and ultrashort pulses (1-200 fs) [24]. The extremely high energy densities are used to directly ablate localized volumes of material with collateral damage confined within 1-2 µm at ablation fluences that are below 2-5 times the ablation threshold. The coupling of ultrashort femtosecond pulses with kilohertz or megahertz pulse repetition rates provides material removal rates 4-5 orders of magnitude faster than any existing serial sectioning technique. The time consuming nature of 3D dataset acquisition and reconstruction, particularly for volumes in the $\mathrm{mm^3}$ range, motivates this research to develop a better fundamental understanding of laser-material interactions that enabled the increases in sectioning speed.

The FSLSS technique is shown to be suitable for 3D characterization of a range of materials, as discussed in Chapter IV. The material removal rates for the femtosecond laser are significantly faster than mechanical polishing and focused ion beam (FIB) milling.

The reconstructed 3D datasets can be directly used as initial input for models of processing or property prediction, such as ductile fracture and toughness modeling. The overall goals of the research presented in this dissertation are to:

1. Establish a fundamental understanding of material removal under the action of ultrashort pulses deposited on multiphase materials;

2. Develop a technique utilizing a femtosecond laser for tomographic analysis;

3. Demonstrate the utility of the technique for acquisition of 3D datasets that provide input to material property models.

1.4 Computational Power and Data Storage

The amount of storage required for high resolution 3D datasets has grown to be at least 100 megabytes/slice for each detector source, often with hundreds to thousands of slices (with a single imaging source, 10-100 gigabytes). Only in the last 10 years have desktop computers become powerful enough to deal with these storage and the corresponding computational demands. Given the deficiencies of sample characterization in 2D, recent increases in computation processing power, the advancements in cameras and imaging techniques, it is now feasible to consider more routine collection of structural information in 3D, along with reconstruction and further computational analysis using the 3D information.

Digital imaging devices such as charge coupled device (CCD) or complementary metal-oxide semiconductor (CMOS) cameras have experienced exponential pixel density growth in sensors for the last ten years. Techniques that rely on CCD or CMOS sensors, such as: optical microscopy, tunneling electron microscopy (TEM), and electron backscatter diffraction (EBSD) all continue to produce larger sized images with higher resolution. This result has the following effects, (1) producing datasets with higher resolution and therefore increased computational requirements and (2) requiring larger sized media storage for archiving and analyzing the data.

Dataset size scales with the resolution of each image and the number of slices collected, also called the sectioning resolution. Using only one imaging source, such as optical microscopy, can yield datasets with slice sizes of 100 megabytes with hundreds of slices per dataset, or roughly 10 to 50 gigabyte datasets. When multi-modal data

is collected, datasets will proportionally scale larger with the number of data types collected. As data requirements have become larger, magnetic media storage density continues to increase by a factor of 10 every 3 years [25]. Currently, 3D datasets are so massive that computational power limitations require that they are resolution down-sampled and intelligently meshed [26]. Processing power continues to increase according to Moore's Law, which states that the transistor density will double every 18 months or so [27]. The trends in increases in computational capacity, inexpensive data storage, and digital imaging CCD technology suggests that the potential capabilities of 3D data acquisition tools and the capacity for the analysis, modeling, and simulation of these datasets will continue to become richer in resolvable detail and size.

This thesis is organized as follows. In Chapter IV, a detailed description and the motivation for the development of the new femtosecond laser based serial sectioning (FSLSS) experimental technique, followed by a discussion of the role of TiN particles distributed in a 4330 ultrahigh strength (UHS) steel as they limit fracture toughness (Chapter V). Afterward, a summary of the current accomplishments will be presented (Chapter VII) preceded by a new projected direction for the application of the femtosecond laser: *in situ* machining in an SEM vacuum chamber, discussed in Chapter VI.

CHAPTER II

Background

The oldest known application of mechanical serial sectioning for the acquisition of microstructural information dates back to the work of Otto Forsman in 1918 [28], with reconstruction of pearlite colonies in hypereutectoid steel. More recently, 3D tomographic imaging techniques using electrons, ions, X-rays, electromagnetic fields, and abrasives have been developed [1, 2, 5, 9, 29–40]. Subsequent applications of these new techniques to analysis of steel microstructures include the 3D reconstructions of complex proeutectoid ferrite laths [41], pearlite colonies [31], and coarse martensite [35]. An overview of recent developments in tomographic techniques is given in Section 2.1. The ability to remove bulk amounts of material with negligible local microstructural damage has motivated the application of these lasers as a tool for sectioning material in this thesis. Femtosecond laser-material interactions will also be discussed, in Section 2.3.1, particularly in the context of material removal and multi-phase material ablation. Finally, a review of microstructure of 4330 steel and ductile fracture will be discussed in Section 2.2 to prepare for the example case of toughness modeling presented in Chapter V.

2.1 Existing Tomographic Techniques

The current state of the art serial sectioning techniques, which can address large datasets at microstructural levels of detail, are painstakingly time intensive experiments. In this chapter, only techniques that can address near mm^3 dataset volumes while capturing low volume fraction microstructure detail will be discussed. The three most widely used tomographic methods are: mechanical serial sectioning, X-ray tomography, and focused ion beam (FIB) serial sectioning. Mechanical sectioning is the most commonly used technique because in some instances it not require any expensive or inaccessible hardware; this will be discussed in Section 2.1.3. X-ray tomography systems are becoming widely available and fully automated and are discussed in Section 2.1.2. FIB serial sectioning, Section 2.1.1, is the newest of the presented techniques and has the highest imaging resolution but characterizes the smallest sample volumes.

There are a number of different techniques by which 3D datasets can be collected. These techniques vary in the amount of material that can be removed per slice, the minimum slice thicknesses, the minimum imaging resolution, the maximum volume which can be sectioned, the slice rate, and whether or not the technique is destructive or non-destructive. Many of these techniques, described in more detail in section 2.1.1 through section 2.1.3, are complementary to the FSLSS and have materials and length scales over which they are most effective. A suite of tools is necessary to access and quantify the microstructure that exists across length scales.

2.1.1 Dual Beam FIB

Focused ion beam serial sectioning (FIB) was developed following the advent of the FIB column being integrated with a SEM chamber, a so-called Dual Beam FIB (DB-FIB) [3, 42–44]. A predefined sample geometry is milled into the sample surface so that the stage can be rotated to access all the tilt angles [44] needed for machining

with the gallium ion beam and for collecting microstructural data, such as electron backscatter diffraction (EBSD) data, energy dispersive spectroscopy (EDS) information, or scanning electron microscopy images. Each detector mounted in a DB-FIB occupies a different set of solid angles to gain access to the sample. Accessing the correct geometric planes for data acquisition can be difficult due to the presence of multiple detectors inside DB-FIB chambers, presented in Figure 2.1 [44], and because the detectors require different angles of incidence for data collection. This technique of sectioning is effective for reconstructing small volumes of material (less than 5 μm^3 with slice thicknesses ranging from 5-100 nm, and 6-7 nm/pixel in-plane imaging resolution [3, 39, 42–44]. DB-FIBs make use of machine scripting to automate the SEM acquisition and the FIB machining steps. Fiducial marks are usually scribed into the sample surface to aid in fine-scaled alignment of the tilt angles and sample position from slice to slice. The DB-FIB can acquire SEM image slices of size 50×50 µm at a rate of 25-50 per hour in a fully automated mode. Datasets have been collected from many different types of materials, such as small inclusion phase distributions in steel samples [45], alpha and beta phases in titanium [36, 37], martensite laths in steels [41], and gamma prime precipitate distribution in Ni-base superalloy castings [34].

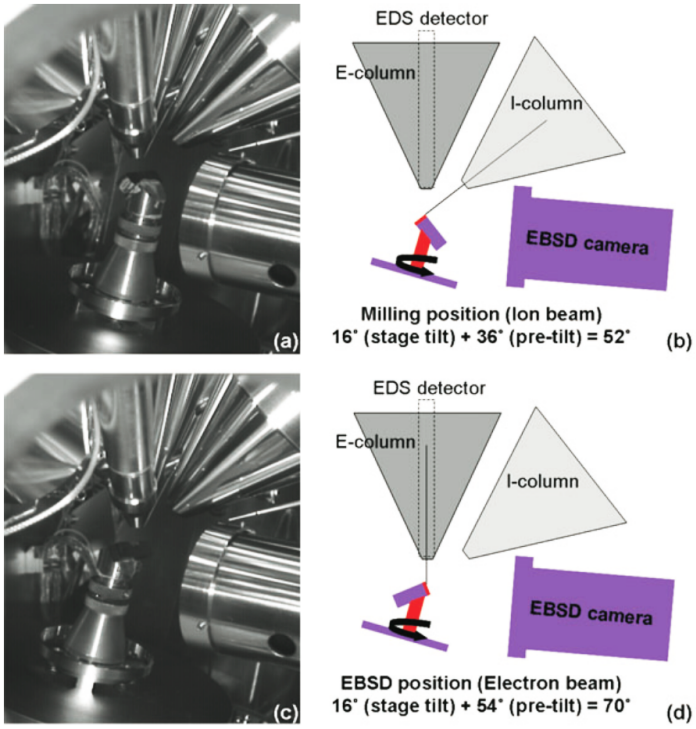

Figure 2.1: Dual-beam FIB stage views (a & c) showing the numerous detectors in proximity of the sample. Schematic sample positions (b & d) during milling and electron backscatter detection EBSD. (Image from G.D. West [44]).

2.1.2 X-Ray Tomography

X-ray tomography is a way of non-destructively generating 3D datasets using high power collimated X-rays. This technique has been packaged into commercially available turnkey systems (SKYSCAN, PHOENIX X-RAY, NORTH STAR IMAGING, and XRADIA), modeled after the medical imaging units, but tailored for micron-scaled resolution of millimeter to centimeter-sized samples. A typical benchtop system has a 150 kV X-ray source that can give micrometer-scale resolution, depending on the density of the material. Unfortunately, the reconstructed volume shrinks as the resolution increases, due to the geometric relation between the magnification and the diverging beam, as shown in the schematic in Figure 2.2 [46]. These systems can readily reconstruct material volumes in the near mm^3 range with 2.5 µm voxel resolution for

phase constituents with high dispersion contrast (such as air/metal or polymer/metal composites). Examples of materials reconstructed using this tomographic technique include ceramic and bioactive glass scaffolds for biomedical applications [47–49], microcracks in steel compact tension samples [50], solidifying dendrites in light metals [51], and casting pores in aluminum [52]. Datasets are captured in approximately 24 hours and reconstructed over the course of a few days processing time. The major limitations of these techniques are the lack of resolution and the low diffraction and phase contrast in thick samples or dense materials. In order to overcome these problems, synchrotron radiation can be used with much higher penetration depths and better imaging resolution due to the enhanced beam collimation and tunable beam energies [53]. For example, Figure 2.3 shows variation in chemical composition in an as-cast superalloy with elemental segregation due to improved phase contrast from the synchrotron X-ray source [54]. Synchrotron X-ray reconstructions also can be 4-dimensional by imaging the time-based evolution of microstructure such as grain growth [55] and aluminum alloy dendrite solidification [56].

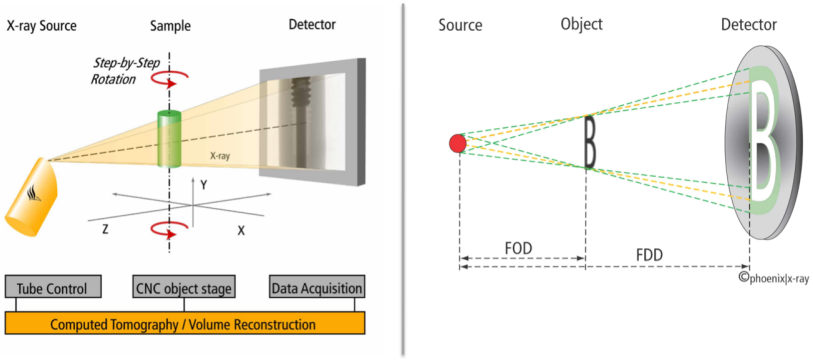

Figure 2.2: (left) Schematic of X-ray tomography setup in which the sample is rotated between the source and the detector. (right) The voxel resolution of the technique is dependent upon the (1) magnification that is determined by the geometric ratio of the focus to object distance (FOD) to the focus to detector distance (FOD), (2) the detector resolution, and (3) the focal spot size of the X-ray source. (Image from O. Brunke [46]).

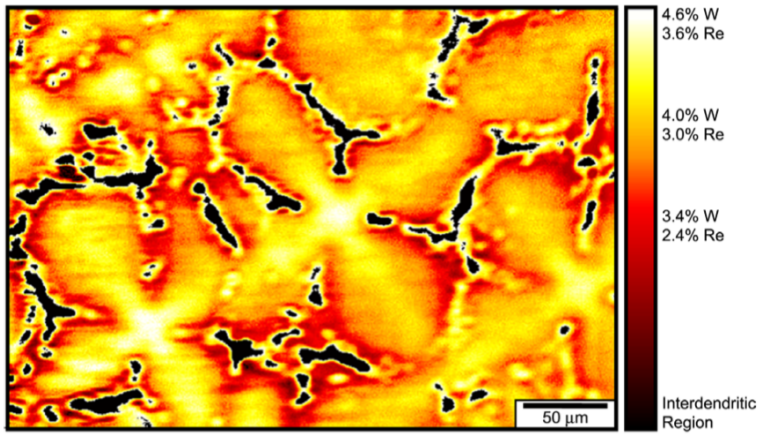

Figure 2.3: Synchrotron X-ray image of Ni-Al dendritic structure. Elemental segregation is shown by false color derived from the varied absorption contrast of the regions. (Image compliment of N. Husseini [54]).

2.1.3 Mechanical Serial Sectioning

The most widely used serial sectioning technique is mechanical polishing. Mechanical serial sectioning techniques use an abrasive medium or a tool bit to remove layers of material from the sample surface between imaging steps. Many different approaches have been employed, including micro-milling [2], mechanical polishing [1, 4, 5, 30, 32, 35, 56], and grinding/dimpling [33]. Accurately monitoring and measuring the material removal rate is a major challenge of all serial sectioning techniques and is specifically difficult in mechanical sectioning due to the direct contact mode of material removal. Consumable milling or grinding media must be periodically replaced or refreshed as they wear during sectioning experiments. To circumvent these problems, many techniques make use of fiducial marks to monitor material removal rates [38, 57], such as micro-indents on the polishing surface or by monitoring geometric patterns scribed on the edge of the sample [35, 37]. The fiducial marks are tracked using pre-determined geometric relations to reconstruct the removal rates after the sectioning. Systems such as RoboMet.3D [4] incorporate automation of the polishing, imaging, and etching steps, although depth profiling and consumables must

still be manually monitored. The automated mechanical polishing serial sectioning techniques, such as RoboMet.3D, can make slices as thin as 0.1 µm for small sample volumes at a rate of approximately 4-20 slices per hour. Optical images or SEM images and EBSD orientation data may be manually collected between slices. Difficulties of mechanically serial sectioned datasets include that they are often difficult to segment and align, and that imaging parameters and imaging areas can shift during sectioning due to human errors and imprecise sample position encoding. These sources of error require advanced segmentation algorithms and occasionally substantial human input for accurate image processing. Voorhees et al [2] made progress in addressing these problems in the image registration steps by equipping the translational stage in their sectioning setup with an encoded transducer. This modification introduced increased repeatability into the spatial location of the imaging area during image capture steps. Rowenhorst's [58] recent work has been aimed at producing the highest fidelity datasets possible. Removal rates are calibrated by scribing FIB markers into the edges of the sectioning experiment samples, and then monitoring their removal during imaging steps. A full-time staff member meticulously collects optical images with supplemental EBSD data. The reconstruction process is extremely time intensive but produces high resolution datasets with multi-modal data (both EBSD grain orientation information and optical microscopy). Figure 2.4 shows a 3D reconstruction of 4380 collected and analyzed β grains in a Ti-21s alloy [58]. The number of faces and grain orientations were measured to determine the triple point geometry and a grain growth rate dependence on the number of faces was established.

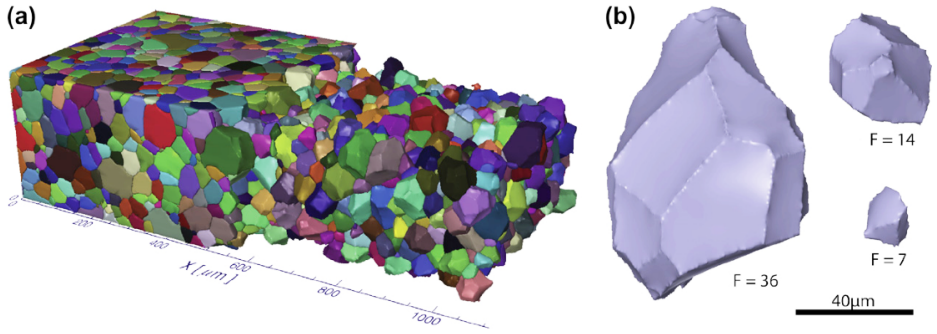

Figure 2.4: 3D reconstruction of Ti-21s. (a) 4380 β grains collected with an entire reconstructed volume of $1115 \times 516 \times 300\,\mu m$ (b) Individual reconstructed β grains of different sizes with the corresponding number of faces annotated [58].

2.1.4 Current Challenges with 3D Tomographic Techniques

Destructive serial sectioning techniques are extremely time intensive. Sectioning experiments require at least days for completion, while the time required to analyze, segment, mesh and reconstruct the captured dataset will take weeks to months to complete. For mechanical sectioning datasets of roughly $1500 \times 1500 \times 300\,\mu m$, collection times will require 2-3 weeks with supervision required to replace consumables. Focused ion beam sectioning experiments of size $50 \times 50 \times 50\,\mu m$ will require roughly 4 days for collection [42]. Therefore, steps should be taken to reduce processing time during the experimental setup by increasing imaging fidelity or by capturing from multiple data sources. Furthermore, consistency in imaging parameters such as contrast, brightness, color balance and imaging area will all help reduce in processing time.

2.2 UHS Steel

Throughout the past three decades, extensive research efforts have aimed to better understand the process of fracture and failure in high toughness metals, such as steel. In tough materials, cracks are initiated and propagate from flaws or locations of high

stress concentrations with a high degree of energy absorption. In structural materials, flaws include porosity, carbides, nitrides, or other inclusions where the second phase cannot compatibly deform with the matrix phase. Therefore, the orientation and distribution of these defects can dramatically change the fracture process. Tomographic techniques provide unique 3D data that can address these complex fracture problems.

2.2.1 Applications and Background

Ultrahigh strength (UHS) steels were developed for applications requiring high strength, toughness, and wear resistance. Applications for these materials include naval and other military armor, structural aerospace components, and impact resistant applications where brittle type failures are not acceptable. They are useful in structural applications at ambient to slightly elevated temperatures (150 °C); with waning mechanical properties as the use temperatures approach the tempering temperature.

Armor designed for ballistic penetration resistance typically fails through ductile fracture within bands of concentrated shear Figure 2.5 [17, 59, 60]. Ductile failure is the usual mode of failure in structural metals, with strain energy being absorbed through the process of plastic deformation, void nucleation, growth, and coalescence [11]. Crack propagation in high toughness materials occurs through void nucleation and linkup. Small microvoids tend to nucleate near the interface of primary inclusions and the matrix through a de-bonding event [17]. Propagation of cracks is therefore aided by microvoid linkup in the local vicinities of inclusions. Also, non-uniform particle distributions in regions of localized plastic flow significantly reduce the capability for plastic flow as the volume fraction of particles in the localized regions increases [12, 61–63]. Due to the deformation processing involved in forging, the primary inclusions discussed above tend to be heterogeneously distributed and are poorly characterized by 2D stereological [14, 23, 64] or statistical approximations,

therefore necessitating the collection of large representative volume element (RVE) 3D datasets. Using the FSLSS technique, we investigated the distributions of TiN and Lanthanum Oxy-Sulfide inclusions in a 4330 titanium modified steel and a C-61 gear steel, respectively.

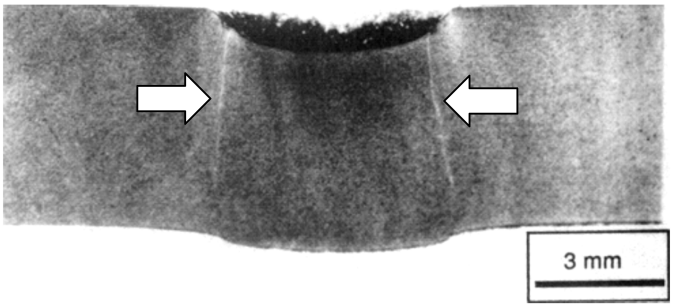

Figure 2.5: A 4340 plate steel after ballistic impact with visible shear localization that is visible in the form of white bands [17]. (Image from J.G. Cowie et al [17])

When chemistry and tempering steps are controlled properly, these types of high strength steels tend to have ductile failures whereby strain is localized into shear bands and energy is dissipated by the generation, growth, and linkup of voids. The development of these highly deformed areas in the material dissipates energy and therefore makes them useful for armor applications.

There are three main classes of UHS steels: high alloy maraging steels, high alloy secondary hardening steels, and low alloy steels. The work in this thesis focuses on a low alloy UHS titanium modified 4330 steel.

2.2.2 Microstructure and Chemistry

The three general classes of UHS steels (high alloy maraging steels, high alloy secondary hardening steels, and low alloy steels) rely on different microstructural strengthening mechanisms to achieve their high strength. Type (1), high alloy maraging steels use intermetallic substitutional compounds such as Ni_3Mo, Ni_3Ti, and $Fe_2(Mo,Ti)$ to precipitation harden its relatively carbon free Fe-Ni martensitic

structure. Type (2), secondary hardening steels use the same basic substitutional compounds as high alloy maraging steels, but also contain chromium, molybdenum, or vanadium carbides that precipitate during a 773-873K tempering step. The intermetallic carbides usually replace cementite phases during the tempering step. Type (3), low alloy steels are martensitic mid-carbon tempered steels that form intermetallic or transition metal carbides during a low-temperature tempering step at up to 523K.

UHS steels are primarily composed of either Fe-Ni or Fe-C martensitic microstructure. Martensitic steels require a fast quench from an austenitic solution to form their metastable body centered tetragonal (BCT) crystal structure. The structure of consists of a solid solution of the alloying components (C or Ni) that are diffusion limited during the fast quench. Specifically, super saturated carbon is trapped interstitially in the BCT crystal structure during martensitic transformation. Carbon is the most potent strengthener added to steels, as shown by the classic work of Winchell and Cohen [65]. The martensitic steel microstructure has high strength and hardness but is inherently brittle from either the high residual stresses of quenching or substitutional element lattice mismatch.

Martensite is formed during a fast quench from solutionized austenite. In low-alloy mid-carbon steels the martensite microstructure is composed of packets of elongated parallel lath structures. These martensite packets and laths are proportionally sized to pre-quenched austenite grains (Figure 2.6) [66]. Given the high hardness of martensite due to the supersaturated carbon content, tempering steps are often applied to precipitate carbide strengtheners and increase ductility through the formation of cementite. The schematic in Figure 2.7 [67] shows the carbon concentration profiles and the corresponding microstructural evolution of tempered martensite. In Figure 2.8 [68], an optical micrograph of a martensitic steel with an etched microstructure is shown. No carbides are present with a fairly homogenous lath martensite microstruc-

ture present. An optical micrograph of a similar martensitic steel after tempering is shown in Figure 2.9 [69] with clearly developed carbides mixed with cementite.

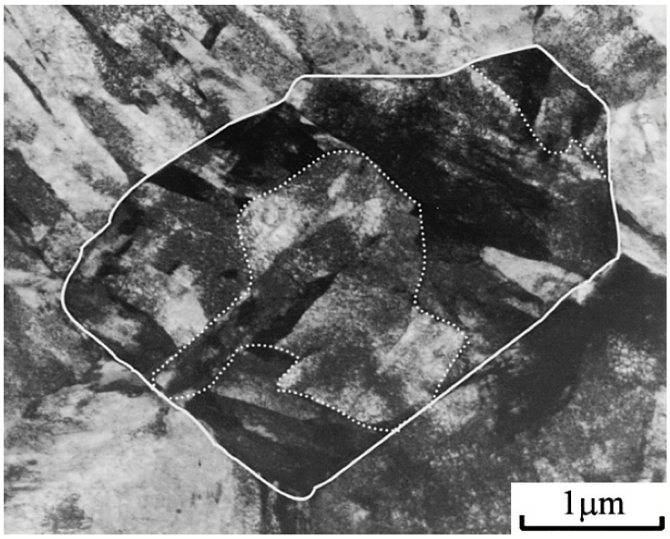

Figure 2.6: A TEM image showing prior austenite grain size (in solid white lines) and martensite packet laths (in dashed white lines) in a Fe-0.2C-1.5Mn-0.15V steel with grain size of 2.3 μm. (Image from S. Morito [66])

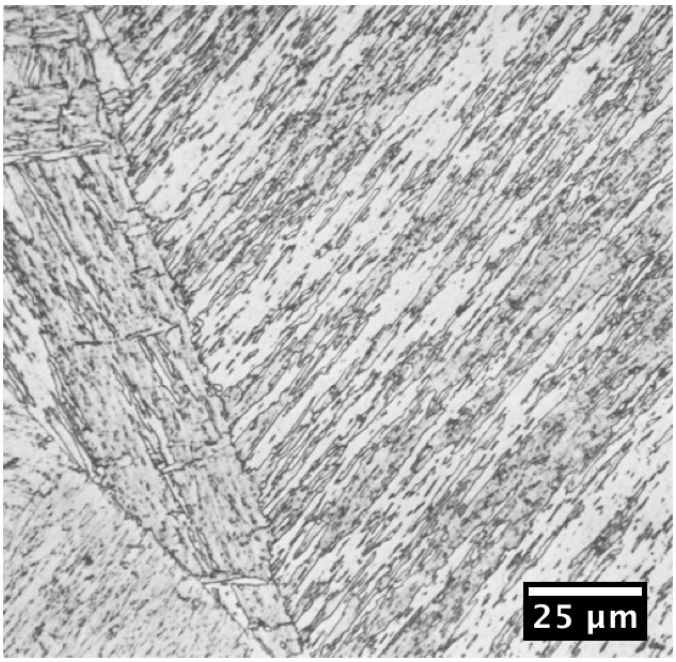

Figure 2.8: An optical micrograph showing the lath martensite structure for a low-temperature (200 hr at 400^o C) heat treatment. Martensite is present without any visible carbides or cementite. Image from R.N. Caron [68].

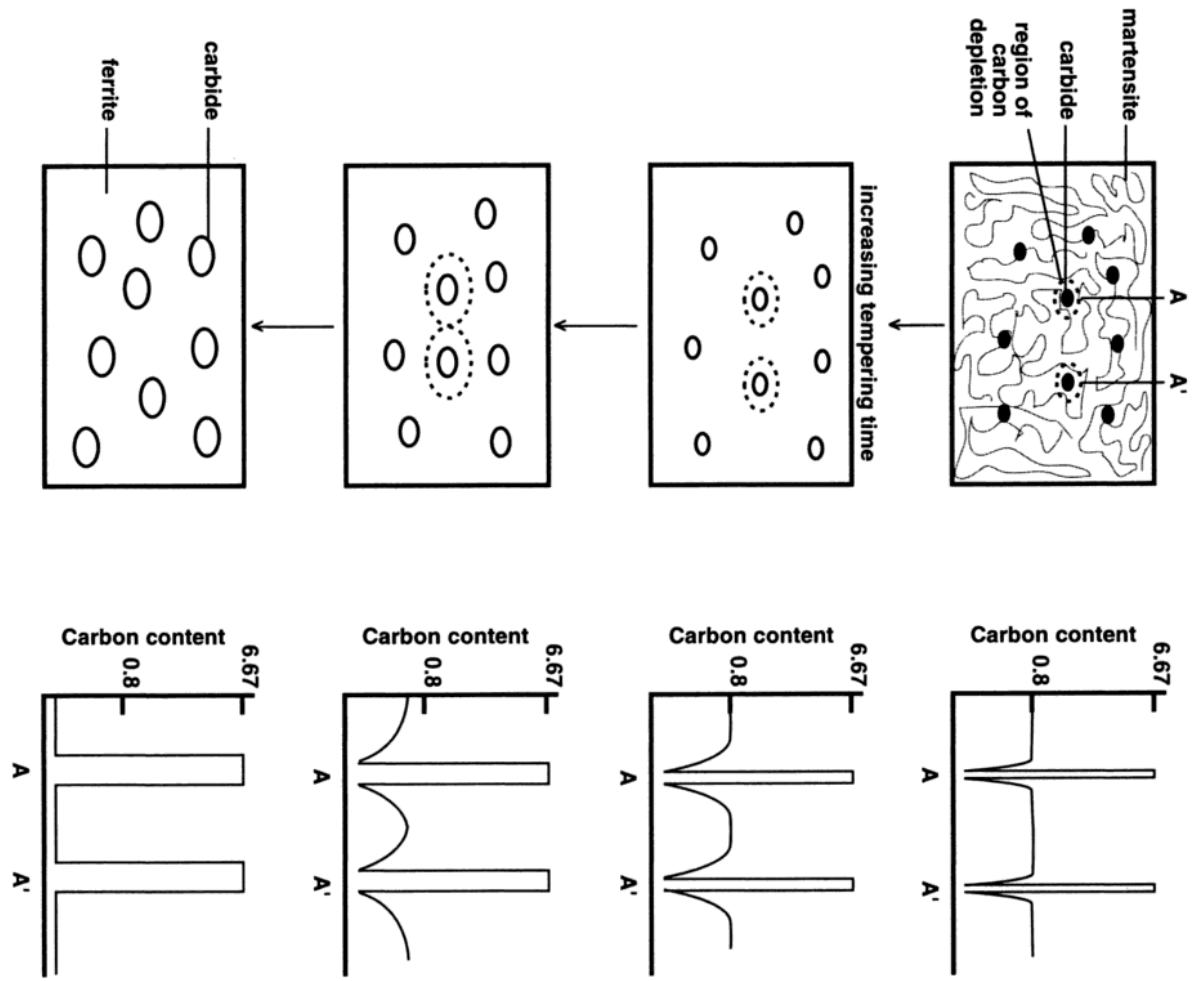

Figure 2.7: A schematic showing the formation of carbides during the tempering process in martensitic steels and their corresponding carbon concentration profiles. Image from C. Brooks [67].

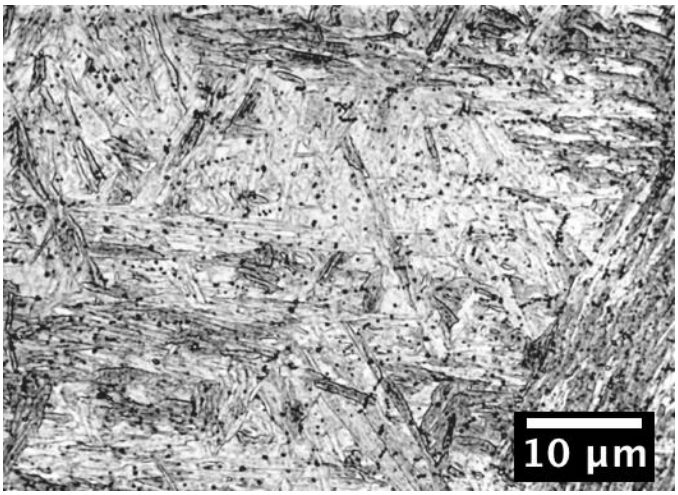

Figure 2.9: An optical micrograph of tempered martensite with carbides and cementite present near retained austenite grain boundaries. Image from B. Bramfitt [69].

In most engineering materials inclusion phases or precipitates exist. High strength steels are no exception, generally exhibiting small, sub-micron precipitate strengtheners formed during tempering, as well as larger 1-50 µm particles precipitated during quenching from solution. The larger particles tend to exist as unintentional ceramic phases, which are generally detrimental to properties such as toughness and strength because they facilitate the process of ductile fracture by nucleating voids at the matrix interface. The inclusion particles also create stress concentrations between the particle-matrix interface due to non-uniform deformation of the two phases. Non-metallic particles have been shown to deform elastically while the matrix deforms plastically, fracturing particles or causing decohesion. Both lead to microvoids that are detrimental to strength [18, 70–72]. Furthermore, some large non-metallic particles have been shown to be particularly susceptible to void nucleation by particle fracture [72, 73]. This large particle effect is often justified by the greater presence of surface flaws in the these brittle particles, leading to lower stresses required for particle fracture [72].

Carbides and nitrides can be distinguished, respectively, by their spherical and

cuboidal geometry from the micrograph in Figure 2.10. Ductility and toughness are enhanced in these steels by precipitating transition carbides during tempering step(s). Carbide precipitation is driven by the fast diffusion of the super-saturated carbon from quenched martensite microstructure, which occurs at elevated temperature due to the metastable nature of the martensite. Cementite (Fe_3C) can also precipitate on the grain boundaries during tempering step(s) if the amount of carbon is greater than 0.5 weight%. This process is referred to as martensite embrittlement. In steels with more complex compositions, tempering steps may be used to form complex carbides or intermetallic phases from other elements in solution.

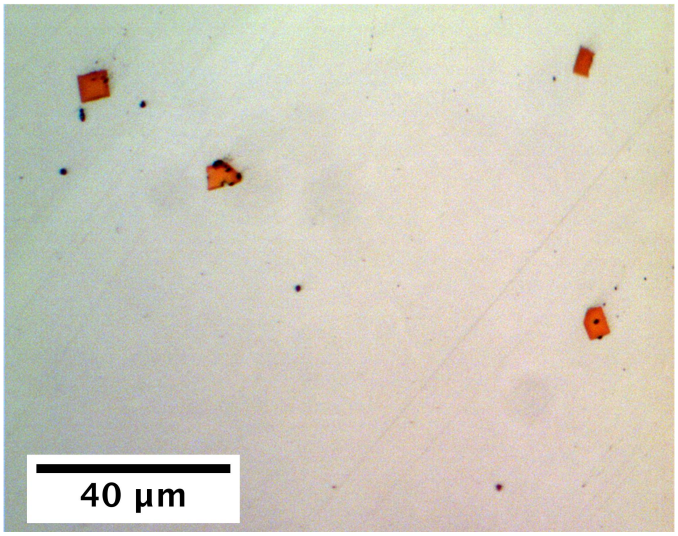

Figure 2.10: An optical micrograph of 4330 steel with cuboidal red-colored TiN particles and smaller round black TiC particles

In this research, we focus specifically on a titanium modified 4330 steel designed for applications that are subject to high strain rate deformation, such as in naval armor and heavy construction machinery. Under these conditions, toughness becomes a major consideration along with strength. The specific chemistry of the low alloy titanium modified 4330 steel is listed in Table 2.1. In Figure 2.11 a FIB etched BSE electron image shows the martensitic microstructure with TiN and TiC precipitates. The microstructure of this high strength steel contains 1-10 µm cuboidal titanium

nitride (TiN) primary inclusions (Figure 2.10 - red particles) and sub-micron TiC secondary inclusions (Figure 2.10 - small black particles). Titanium is added to form sub-µm TiC strengtheners, but also results in TiN particles, which are deleterious to the fracture toughness. The TiN inclusions can be easily identified when imaged optically because they appear red in color due to absorption contrast. The inclusion distribution and the morphology of the inclusions have been shown to affect the void nucleation substantially [11]. Therefore, the 3D datasets have been acquired and assessed statistically for information such as mean particle size, mean nearest neighbor distances, and particle volume fraction.

Table 2.1: Composition in weight % of titanium modified 4330 steel.

(wt%)	C	Si	Cr	Mo	Ni	Cu	Ti	V	P	S	Fe
Mod. 4330	0.29	1.52	1.91	0.38	0.19	0.14	0.042	0.11	0.012	0.005	bal.

Figure 2.11: A BSE micrograph of FIB milled 4330 steel with two cuboidal TiN particles and smaller round dark grey TiC particles. The martensite laths are visible in light contrast grey scales in the background. (Image from M.D. Uchic [45]).

2.2.3 Mechanical Properties

UHS steels are commonly defined to have yield strength of at least 1380 MPa. They are usually tempered in order to increase their toughness and ductility at the sacrifice of yield strength. The titanium modified 4330 (Ti mod 4330) steel has lower yield strength of approximately 1275 MPa as estimated from hardness measurements. The Young's Modulus for this steel is 200 GPa, the Yield Strength is 1206 MPa (175 ksi), and the Ultimate Tensile Strength is 1461 MPa (212 ksi), a hardness of 50.4 HRC, and a Charpy impact energy of 37 joules.

Processing of the 4330 samples included a 1-hour austenizing step at 975°C and a highly agitated water quench. Its mechanical properties established by a 215 °C tempering step at 100 minutes followed by an air cool at which point a Rockwell hardness of 50.4 developed.

2.2.4 Failure Modes

Ductile failure occurs when a material experiences intense plastic deformation before fracture. Simultaneously, a significant amount of energy is absorbed during this process. Materials with high purity, such as single crystal copper, nickel, niobium, and lead have been shown to endure up to 100% reduction in area before failure (Figure 2.12) [74]. Shear bands, such as those in Figure 2.12, are often clearly visible in tensile tests of these highly strained materials. The ability for metals to slip so extensively is an effect of the shared electronic structure that is typical in metallic bonding.

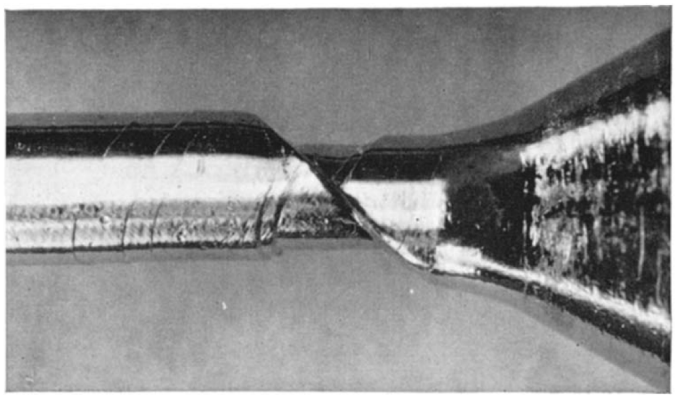

Figure 2.12: Single crystal niobium tensile test specimen showing shear bands and extreme deformation in the gauge section. (Image from C.N. Reid [74]).

A typical ductile fracture in tension is described as having a cup and cone type break. This refers to a necked region where cross sectional area of the specimen has been reduced, a crack has nucleated and propagated internally (usually from the lateral and radial center of the necked region), and failure has occurred within this region (see Figure 2.13). A heavily voided region will form at the geometrical center of a necked region in a tensile sample because of the strong hydrostatic stresses that develop there. The voids in this region connect by continued plastic deformation, and eventually the series of void nucleations and their connectivities will drive the extension of a primary crack or cracks radially outward toward the edges of the necked sample. Multiple void aggregations, referred to as void sheets, zig-zag outwardly at angles of 50-60° radially toward the edge sample. Once the void sheet comes in proximity of the edge of the sample shear stresses begin to dominate and produce a fracture surface running at 45° between the axial and radial directions, developing the cup and cone edges. The fracture surface in ductile failures is described as having a dimpled surface, which is characteristic of the filamented breaks that occur with crack propagation and void linking.

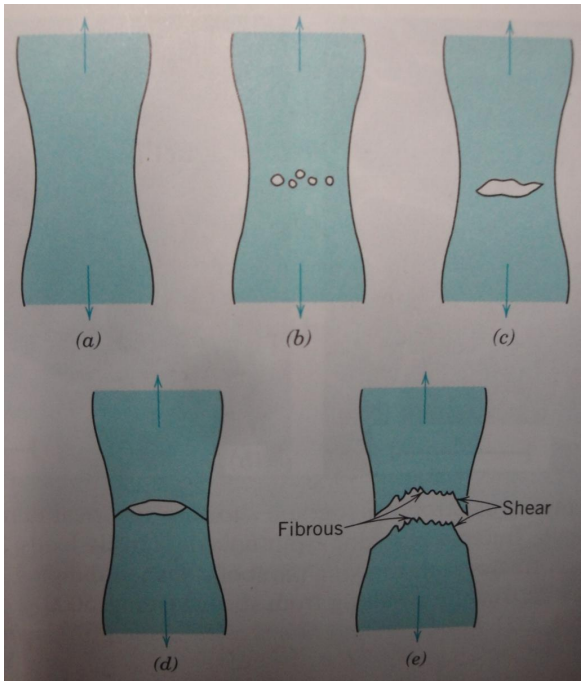

Figure 2.13: A schematic illustrating the ductile fracture process. In (a) a specimen is necking down in the gauge region with greater applied stress. In (b) voids begin to nucleate at the center of the necked region where hydrostatic stresses are the largest. In (c) void-linkup and crack formation occur spreading radially outward toward the edge of the gauge section. Crack propagation tends to follow a zig-zag pattern along paths of greatest shear stresses. In (d) cracks have spread, and therefore cross-sectional area has decreased to a point where high stresses form brittle-type crack propagation. In (e) typical fracture surfaces are illustrated. (Image from T.B. Cox [72]).

Void sheets form along bands of shear that extend from propagating cracks in a stressed material. The shear bands form at 45° to the normal of stress direction, and the crack will tend to follow a zig-zag pattern along these 45° shear bands staying localized to the bar section of highest stress (normally the gauge section with most necking) [75]. The ductile fracture surface usually has a dimpled texture reminiscent of a small forest of necked regions. These dimples result from matrix and second phase plastic deformation incompatibilities. For instance, a hard undeformable inclusion phase will produce a large density of dislocations surrounding it, as the matrix is plastically deformed and the inclusion resists elastically. As plastic deformation continues the second phases may either fracture in a brittle manner or deform plas-

tically, generating voids and microcracks [76]. Therefore, the volume fraction, size, type, and special arrangement of inclusion phases, such as carbides, nitrides, and sulfides, can be of particular importance in dictating the amount of energy dissipated during a ductile fracture. Schematically in Figure 2.13, voids can be seen to nucleate, grow, and propagate, eventually leading to failure within the necked region. In Figure 2.14, work by Cox and Low [72], inclusion phases are visible as void nucleators in the concavity of the dimpled surfaces.

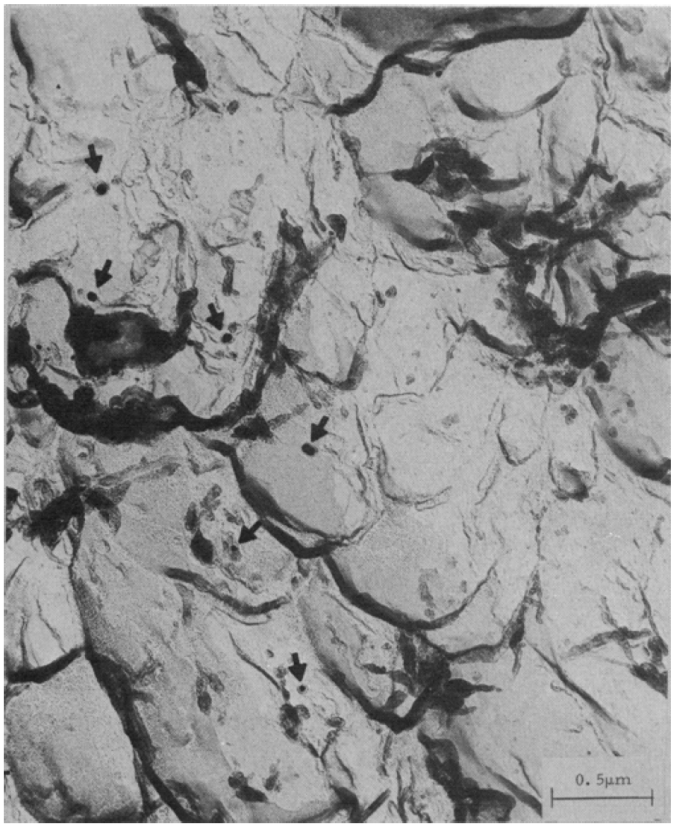

Figure 2.14: SEM image of AISI 4340 steel ductile fracture surface. Nucleating cementite particles are marked with arrows. (Image from T.B. Cox [72].

The toughness of UHS steels is limited by the localization of plastic deformation at, and between, primary inclusion particles such as titanium-nitrides [77]. The fracture or debonding of these TiN particles has been associated with the nucleation of microvoids in UHS steels [59]. Stress concentrations at microvoids developed by

fractured TiN particles drive the linkup with other voided regions through ligament necking or shearing [78]. The heterogeneous stress distributions that occur due to shear localization near TiN particles reduce the fracture toughness of UHS steels [11].

The void-coalescence process can be significantly affected by local material inhomogeneities. Huang modeled the influence of voids and particles on plastic deformation in his 1993 work [12]. He showed that ductile fracture can occur sooner at lower nominal strains with plastic flow localization. Void nucleation and linkup and oriented planes of microvoiding called void sheets are all forms of localization. Heterogeneity in microstructure, such as particle clustering, can produce local stress concentrations, void nucleation, and coordinated void linkups at lower stresses than would be expected for a volume with homogeneous microstructure. In effect, a microstructural heterogeneity such as a particle cluster acts as a larger effective defect. For instance, in shear banding regions with severe strain localization, a 5% increase in inclusion volume fraction can reduce the overall material ductility by a factor of 2 [12]. The 3D spatial distribution of inclusion phases in steels is directly important for toughness and ductility. The degree of inclusion clustering and other material heterogeneities are of importance for void propagation and growth [12], while the 3D geometry (specifically size) of an inclusion affect the particle's fracture strength and its ability to nucleate voids [72]. Weibull determined that larger inclusions will require lower applied stresses and therefore lower strains to be deformed, fracture, or debond from the matrix [79]. Therefore, being able to predict where the largest flaws are, and how they can interact with each other, is fundamentally important to predicting how to process and modify the distribution detrimental phases like large inclusion particles. In order to characterize the distribution of detrimental TiN precipitates that form in a 4330 steel, an improved serial sectioning technique was required to collect large near mm^3 volumes of material with nm to µm scale resolution.

2.3 Femtosecond Lasers

The advantages of femtosecond lasers for micromachining have motivated the present development of the femtosecond laser based serial sectioning (FSLSS) process. Schawlow and Townes developed the first laser at Bell Labs in 1958 using a potassium vapor gain medium [80]. Since then, a variety of laser media have been developed with pulse durations ranging from continuous wave operation down to femtosecond pulse widths. Femtosecond lasers are particularly of interest because of their pulse-width is on the same time scale, or shorter, than fundamental electronic-ionic material interactions such as the electron relaxation time [81]. Applications for these lasers include: the imaging of events that occur on ultrashort time scales (ablation, plasma generation [82], two photon absorption [83]), diagnostics of highly localized plasma generation (laser induced breakdown spectroscopy LIBS [84]), and low damage laser micromachining [85].

The unique properties of femtosecond lasers stem from their characteristically short pulse-width, high focused intensities, and kilohertz repetition rate. In the following sections, the fundamental characteristics of femtosecond lasers are discussed, as well as the mechanisms by which energy is transfered to electron and ionic species, and an overview of the laser-material interactions including laser ablation and damage thresholds. These unique properties are central to the new FSLSS technique used to perform microstructural characterization in 3D.

2.3.1 Laser Characteristics

High pulse energy (>0.1 mJ/pulse) femtosecond lasers have become commercially available in the last two decades (1987 Clark MXR) with the advent of the chirped pulse amplification (CPA) technology [86]. Previous to this invention, the damage threshold fluence of the optics and gain media limited the amount of amplification in short pulse laser systems. In CPA lasers, see Figure 2.15 [86], a pulse is spectrally

and temporally stretched into the range of hundreds of picoseconds. The different wavelength components in the spectral range are propagated over a widened temporal space allowing for their amplification without self-focusing or optics-damaging beam fluences. Recompression of the beam is performed after the amplification to combine the ultra-short pulse characteristics with the increased beam power. Modern gain media for CPA type femtosecond lasers include solid state Ti:sapphire rods and Ytterbium-doped fibers. Ti:sapphire lasers generate ultrashort pulses by self-mode-locking, a process by which pulse generation is promoted in specific phases through constructive interference, schematically shown in Figure 2.16 [87]. CPA increases the power of Ti:sapphire pulses into a range where they can be used to develop plasmas and laser machine metals and ceramics. Femtosecond lasers produce tightly focused and temporally short pulses with high repetition rates. Unlike laser pulses that are nanoseconds or longer in duration, femtosecond pulses can ablate material with very limited surrounding collateral dislocation damage and very little residual melted material [88]. In Figure 2.19, SEM images of laser drilled holes shows damage increase with increased pulsewidth. Heating is confined to a very localized area in the immediate vicinity of the pulse [89, 90]. Even at high repetition rates (1 kHz to 30 MHz) the time between each pulse delivery is very long, when compared to the 150 femtosecond pulsewidth. Intensities of $> 10^{18}$ W/cm^2 can be achieved by tightly focusing the beam down to 1-10 µm full-width-half-max (FWHM) spot sizes using simple optics such as a doublet lens. Kilohertz repetition rate lasers are available with pulse energies near 3-5 mJ. Recently, megahertz repetition rate lasers have become commercially available with pulse energies of approximately 100 nJ (CLARK MXR, COHERENT).

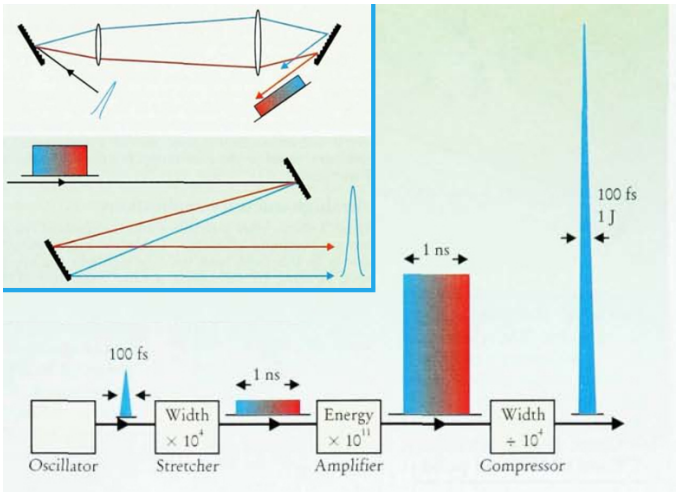

Figure 2.15: Schematic of (a) Pulse stretcher - two opposed antiparallel diffraction gratings with a telescope positioned in between them. An incoming pulse is chirped across its wavelengths with red having a shorter path than blue wavelength. Schematic of (b) Pulse compressor - two parallel diffraction gratings in which the blue has a shorter optical length than red wavelength. Schematic of (c) Temporal ranges of pulse widths throughout the chirped pulse amplification (CPA) process. (Image from G. Mourou [24]).

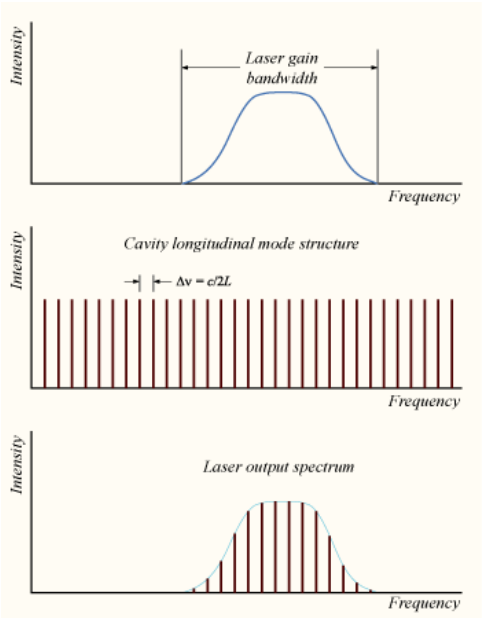

Figure 2.16: Simple example of the laser gain bandwidth, a mode-locked cavity, and the corresponding laser output.

2.3.2 Ablation/Energy Transfer

The dynamics of the mechanism of ultrashort pulse laser material removal has been discussed in theories such as the Two-temperature model [91, 92]. This model is used to predict the electron and phonon temperatures that develop during and immediately after laser pulse deposition. The model assumes that electron excitation occurs through the absorption of the laser photons followed by a localized thermalization of that energy. The thermal energy diffusion is defined by a set of differential equations that govern the temperature gradients based on position and time. Laser ablation is modeled to occur anywhere the local equilibrium temperature exceeds the enthalpy of vaporization for the material. At high laser fluences the Two-temperature model does not agree well with the ablation events produced experimentally, suggesting that mechanisms other than thermal ones are active [93]. Shock melting may be an integral part of the material removal at higher fluences [94]. The model of Torralva *et al* [94] predicts that additional material is removed at high laser fluences due to shock-melting produced by a rarefaction wave caused by the high pressures induced by high velocity material ablatants. This model also predicts that an abrupt change in ablation fluence rate, known as the low to high fluence transition, corresponds to the onset of shock-melting in nickel, aluminum, and a nickel-base superalloy. The generally emerging view is that the following events occur during the laser-material interaction with femtosecond pulses [81, 95, 96]. Initially, ultrashort pulsed laser energy is coupled to the electrons from the incoming photons immediately upon pulse deposition. Femtoseconds later, electron diffusion occurs and the non-equilibrium electron energy distribution relaxes back into a Fermi energy distribution. The electron energy is converted into phononic energy in the next 1-10 picoseconds, which is commonly referred to as the thermalization time or the electron-lattice relaxation time [97, 98]. At this point, ablation occurs as ions are excited to temperatures that are well above their vaporization point. Interestingly though, the laser pulse arrives and

ends picoseconds before any phononic heating begins. This means material ablation, plasma formation, and the corresponding photon emission all occur long after the direct laser light interaction. Diagnostics tools such as spectrometers take advantage of the pulse-ablation temporal gap and are used directly to image the plasma-photon emissions without imaging the laser light. Material removal also enhanced by the pulse-ablation separation time and the subsequent wait time (before the next pulse) in which plasma formation and dissipation can occur.

Femtosecond laser micro-machining experiments have been performed for a wide range of materials to discern the benefits of ultra-short, high intensity laser pulses. These experiments usually involve hole drilling [85, 99, 100], trench fabrication [101], or single pulse laser modification [82, 88, 102]. However, the dynamics of damage formation associated with these laser machining processes has not been studied in as much detail.

Recently, experiments have been performed to quantify the extent of dislocation injection or other forms of damage after irradiation by femtosecond laser pulses. In the work of Kumar *et al*, the extent of dislocation injection into the bulk of nickel base superalloy was measured by cross sectioning single laser pulses irradiated incident to the sample surface [103]. In Figure 2.17 we show EBSD measurements taken from the cross sections to determine the amount of strain induced beneath the laser ablation events. The sample was polished using a Bueler Vibramet polisher to significantly diminish any residual strain fields from the mechanical preparation steps. Similar procedures were followed when sectioning the sample laterally for the same regions. The amount of strain can then be correlated with the density of dislocations necessary to deform the matrix, estimated using EBSD misorientation information. Kumar found that dislocation densities on the order of 2.8×10^{10} per cm^3 were present near high fluence laser craters of $5.1\,J/cm^2$ [103] compared to densities of 10^8-10^9 per cm^3 in undamaged material [54].

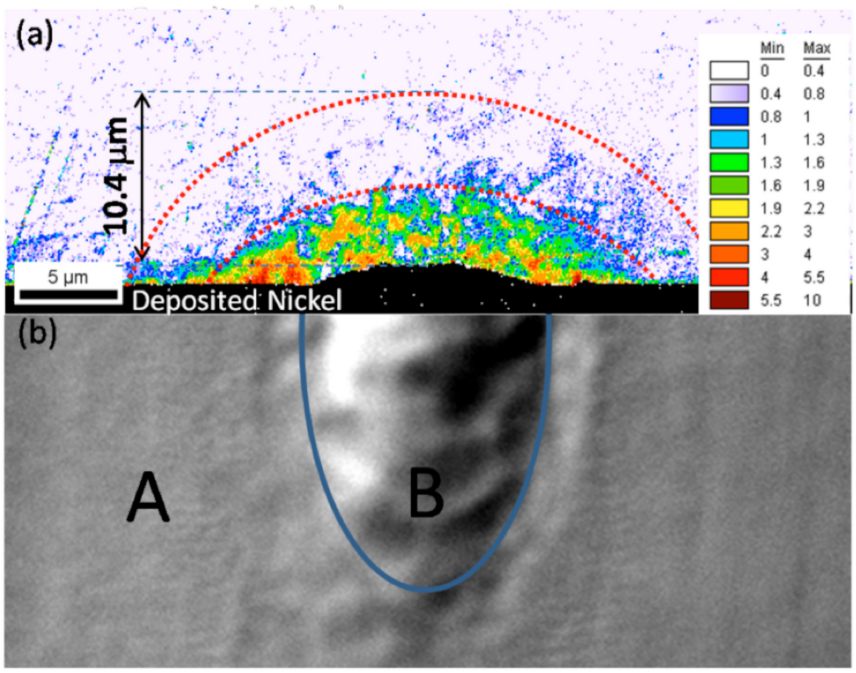

Figure 2.17: EBSD map of a cross-sectioned single femtosecond laser pulse in a CMSX-4 superalloy. Dislocation densities of 2.8×10^{10} per cm^3 have been estimated from the measured strain. (Image from A. Kumar [103]).

Dislocation distributions were analyzed by Ma *et al* in thin sheets subjected to ablation following single pulse laser machining a TEM foil and imaging the region surrounding the damage [88]. Dislocation densities of 10^{10} per cm^2 were measured in an area irradiated with approximately 2.5 J/cm^2. Interestingly, the gamma/gamma' two-phase structure typical of precipitation strengthened nickel base superalloys is unperturbed by the dislocation injection, and are totally unaffected at a distance of 1-2 µm from the edge of the laser pulse, see Figure 2.18 [88].

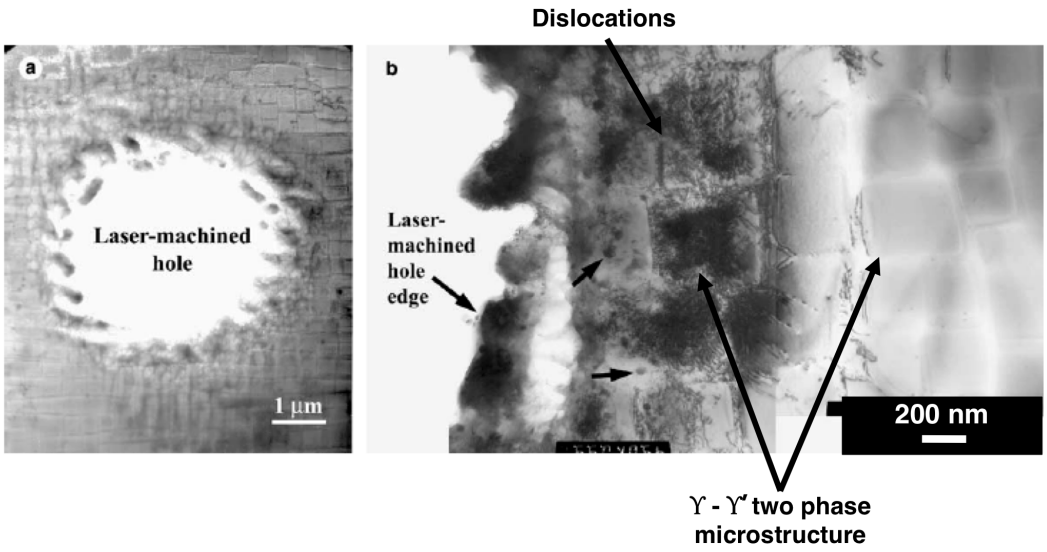

Figure 2.18: TEM images prepared from a foil of CMSX-4 superalloy that was subsequently laser machined with low-fluence laser pulses ($0.392\,\mathrm{J/cm^2}$) [99]. Dislocations extend radially less than 1-2 µms and the $\gamma - \gamma'$ two phase microstructure is unperturbed.

2.3.3 Femtosecond Laser Machining

Femtosecond lasers have been shown to significantly limit material damage during ablation. A number of studies have shown various ways by which these characteristics can be utilized. These include: high aspect ratio hole drilling [88, 99, 104, 105], trench machining [101, 106, 107], laser induced breakdown spectroscopy (LIBS) [84, 88, 108–110], and surface texturing [111–113].

In Figure 2.19, SEM images show laser machining with decreasing pulse durations. Continuous wave lasers show the most residual damage and the largest heat affected zone, while femtosecond lasers show the least. Material removal happens between pulses while the laser has stopped pulsing, which gives the ablatants time and a ballistic pathway to eject from the areas that are being laser machined [93, 114, 115]. Energetically, pulsed lasers prevent repulsing of ejected ablated material and provide time for material response [114].

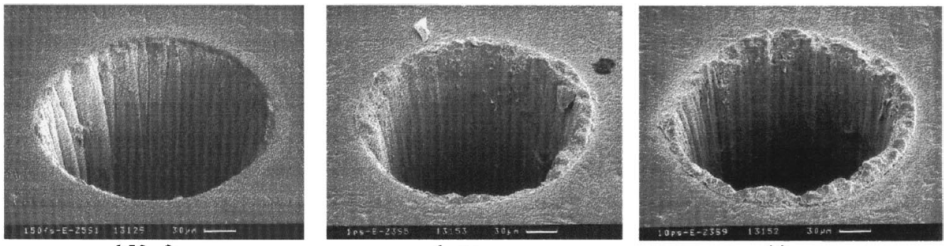

Figure 2.19: Femtosecond laser hole drilling is shown to produce less residual damage and a smaller heat-affected-zone (HAZ) than longer pulse laser machining and continuous-wave (CW) lasers. Laser machined holes using 780 nm wavelength at (right) 10 picosecond pulsed laser, a (middle) 1 picosecond pulsed laser, and a (left) 150 femtosecond pulsed laser [116].

2.3.4 Damage Thresholds

The laser damage threshold is defined as the incident fluence required for single pulse removal of material from a sample surface [96, 102]. The extrapolation of the damage threshold is only as accurate as the quality of the data collected from the imaging techniques used to characterize the damage morphology. Damage has been reported as the maximum depth of material removed in a laser crater, as the 2D damage area, or as the diameter of the laser spot damage area [96, 117–120]. Techniques such as atomic force microscopy (AFM), confocal microscopy, and profilometry can be used to quantify the depth of ablation craters made with various pulse energies. Traditional 2D imaging techniques such as optical microscopy and scanning electron microscopy (SEM) are used to profile the area of the laser pulse crater. A Gaussian distribution is usually fit to the profile of the damage area.

In many materials [85, 88, 96, 117, 119] another high fluence threshold exists as denoted by an abrupt change in the rate of material removal due to femtosecond laser ablation. This threshold will be referred to as the low to high fluence ablation threshold, and is depicted in Figure 2.20 [100, 119, 121–123]. The single pulse damage morphology is qualitatively different when comparing the two regimes. At low fluences, material is generally removed with little or no localized melting and little

dislocation injection [88, 99]. In the high fluence regime, more material per pulse is removed with some short-range melting or re-solidification and a higher degree of dislocation injection [88]. High fluence damage is particularly evident in multi-pulse drilling studies (Figure 2.21 and high-resolution SEM images (Figure 3.10 - left). Damage thresholds are also dependent on the laser pulse-width, for instance, Bonse's work shows that as pulse width is shortened from 200 to 5 fs the ablation threshold decreases by a factor of 2 [102].

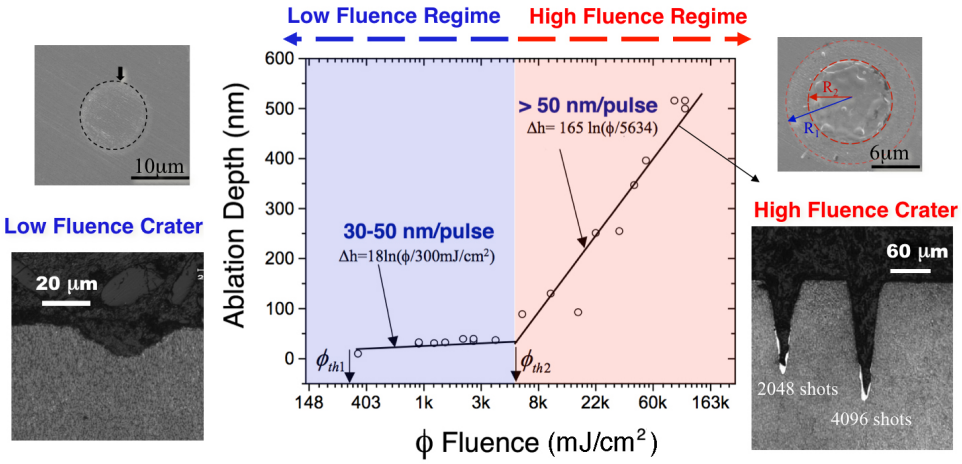

Figure 2.20: Ablation depths plotted for a range of fluences in CMSX-4 superalloy. Corresponding low and high fluence single pulse laser craters are shown in the upper left and right. Material removal rate slope is low for the low fluence range compared to the high fluence range (Image from S. Ma [88]).

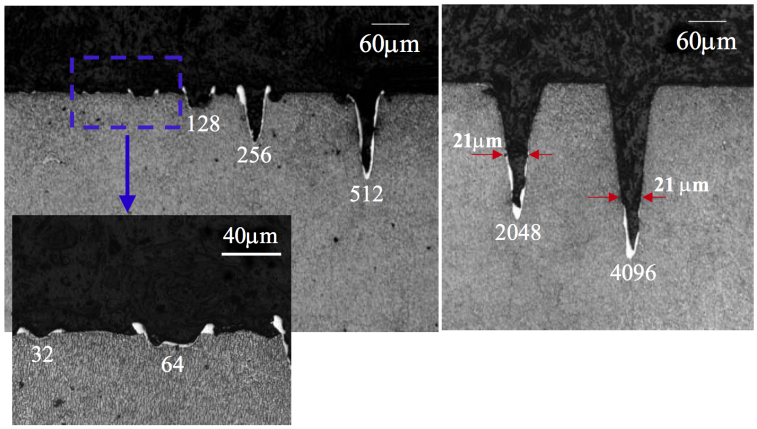

Figure 2.21: Femtosecond laser drilled hole with a high aspect ratio and then sectioned laterally [88]. The SEM image shows low amounts (less than $1-2\,\mu m$ of redeposited material are present on the sides of the sides and the shoulder of the hole. Laser machining was performed with the number of pulses indicated in the image, at a fluence of $12.9\,J/cm^2$.

CHAPTER III

Laser-Material Interactions

Femtosecond lasers are pulsed lasers. Therefore, it is of benefit to study the fundamental interactions of single pulse laser-material irradiations. In this chapter, single pulse laser studies will be discussed in Section 3.1 followed by a description of a more detailed investigation of single pulse ablation in 4330 steel and titanium nitride in Section 3.2. In Section 3.3 the transition from single pulse laser ablation to bulk material removal is considered.

3.1 Single Pulse Laser Studies

The study of the interaction of individual laser pulses with the incident material is important in order to characterize the ablation morphology, evaluate the laser damage thresholds of the material, and to determine the laser-energy distribution on target. Figure 3.3 and Figure 3.10 show optical microscopy, SEM, and AFM images of laser pulse craters with fluences listed in the figure captions. The extent of damage can be fit to the corresponding theoretical Gaussian beam spatial intensity profile to extract valuable parameters such as the focused beam diameter and the corresponding ablation damage thresholds [114].

The peak laser fluence on target is defined as:

$$\phi_{peak} = \frac{E_0}{Area} = \frac{2E_{pulse}}{\pi w_0^2} \tag{3.1}$$

where ϕ_{peak} is the peak fluence, E_0 is the peak pulse energy, E_{pulse} is the average pulse energy, and w_0 is the focused beam diameter.

From the single pulse ablation morphology, a set of scan parameters can be designed to optimize material removal and minimize surface roughness. The laser-material damage studies are also used to determine the laser fluence parameters at which the least damage is subjected to the material with the greatest material removal rate.

Experimentally, single pulses were irradiated on the surface of a sample with spacing roughly 2-3 times the laser spot size diameter to produce a grid of damage spots without impingement, shown in Figure 3.1. Each spot was interrogated using optical microscopy, SEM, atomic force microscopy (AFM), and laser profilometry to determine the ablation morphology. The 2D pulse area was measured by all of the aforementioned techniques, while the ablation depth was measured exclusively using AFM or laser profilometry.

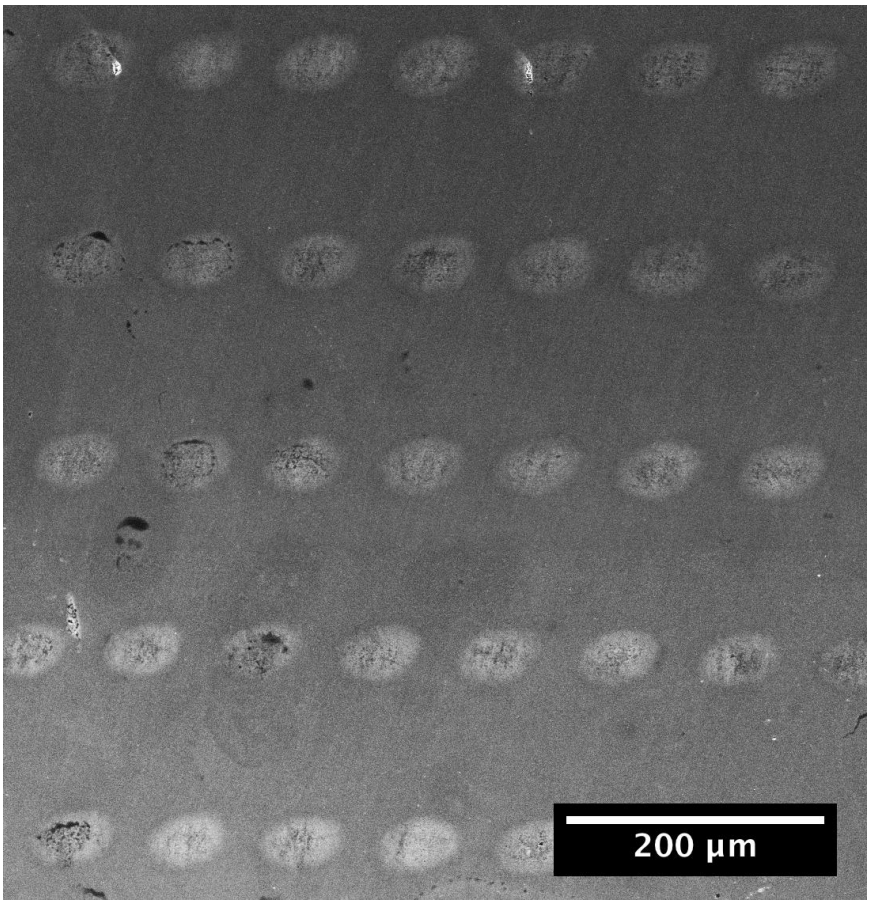

Figure 3.1: SEM image of single pulse laser machined spots on an area of 4330 steel.

For most single pulse studies, a 20 cm focal length plano-convex lens was used to bring the laser into focus on the face of the sample surface. Rough focus was found using a fluorescent card to indicate, by eye, the stage position with minimum spot size. Optimal focus was achieved by laser machining incrementally positioned spots on the sample surface in front of and behind the coarsely determined peak focal plane. The focused beam profile of the femtosecond laser after a 20 cm focal length lens is shown in Figure 3.2.

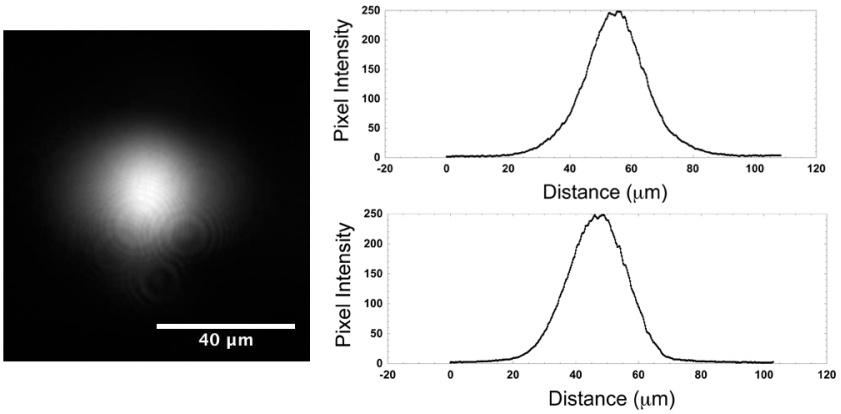

Figure 3.2: CCD image of a the femtosecond laser beam at focus after a 20cm plano-convex focal lens with Gaussian beam profile. The $(1/e^2)$ spot size is 39.05 µm.

Ablation thresholds were estimated from the measured squared diameter data by extrapolating a fit of the lower fluence data points to 0 J/cm^2. The squared diameter is shown to have a linear dependence, for low irradiation fluences, with the log(Laser Pulse Energy). A 2-parameter fit equation shown in 3.3 is used following Bonse's 2001 techniques [124] to determine the ablation threshold ϕ_{th} and the $(1/e^2)$ spot size (w_0).

For a Gaussian beam, Equation 3.2 describes how the energy intensity decreases radially from the maximum at $r = 0$. The parameter w_0 is the $\frac{1}{e^2}$ radius of the intensity distribution and ϕ_{peak} is the maximum laser fluence.

$$\phi(r) = \phi_{peak} e^{\frac{-2r^2}{w_0^2}} \tag{3.2}$$

For a Gaussian beam the Equation 3.3 can be used to fit in terms of E and D^2 to extract the laser threshold damage radius w_0 and threshold ablation energy E_{th} [124, 125].

$$D^2 = 2w_0^2 \ln \frac{\phi}{\phi_{th}} = 2w_0^2 \ln \frac{E}{E_{th}} \tag{3.3}$$

Equation 3.4 is used to calculate the peak pulse fluence ϕ_{peak} as a function of pulse energy E_0 and the laser spot radius w_0.

$$\phi_{peak} = \frac{2E_0}{Area} = \frac{2E_{pulse}}{\pi w_0^2} \tag{3.4}$$

Or by substitution of $E_{pulse} = \frac{<P>}{RR}$, where R.R. is the repetition rate of the laser and $< P >$ is average power, an equation was generated that uses a simple power measurement to calculate peak fluence.

$$\phi_{peak} = \frac{2 < P >}{R.R.\pi w_0^2} \tag{3.5}$$

The average laser output power $< P >$ is measured using a OPHIR 3-watt thermopile powermeter before single pulse irradiation. The $(1/e^2)$ diffraction limited focused laser beam spot size is measured using a Dataray Beam Profiler CCD camera. Using the average power $< P >$, the laser pulse repetition rate (R.R.), and the focused laser spot size $(1/e^2)$ or the measured damage area (w_0), the single pulse energy and pulse fluence can be calculated using equation Equation 3.5.

Arrays of single pulses are deposited on a sample surface for analysis by optical microscope, SEM, AFM, and laser profilometry. Pulses were irradiated on the sample by one of two ways: (1) scanning the sample at a faster constant velocity than the repetition rate of the laser with a synchronized mechanical shutter or (2) by modulation of the internal Q-switch in the Clark MXR femtosecond laser. For case (1): a THORLABS optical chopper was used to reduce the repetition rate of the laser by mechanically blocking some of the laser pulses. An electronic TTL trigger signal is sent to a UNIBLITZ mechanical shutter controls at the same time as the laser Q-switches with an injection pulse. The trigger signal provides ample time for the mechanical shutter to open and shut, only letting one pulse through, without aperture clipping the beam. For case (2): single pulse modulation is controlled through the

hardware controls of the laser, significantly simplifying the setup. Single laser pulses are generated by energizing the Pockels cell long enough for one single seed pulse injection into the main Ti:sapphire gain cavity. A digital interface card provides a TTL signal to the laser for Pockel's cell control. A three-axis Newport programmable mid-range travel stage was used to control sample positioning and motion between single laser pulse irradiations in both cases. Laser beam attenuators were used to access a wide range of laser fluences for single shot laser experiments. Neutral density filters as well as a polarizer-1/2 wave plate were used to attenuate the laser power.

3.1.1 Morphological Characterization

Single pulse laser shot morphologies were characterized using scanning electron microscopy (SEM) and light optical microscopy (LOM) with Nomarski polarized filters. A PHILLIPS XL30 field emission gun (FEG) equipped electron microscope was used to characterize the precise structure, damage thresholds, and geometry of laser damage. LOM was used to survey the general size and distribution of pulse depositions. Nomarski mode polarizers greatly enhance residual matrix strain immediately within and surrounding the laser shots. The laser beam profile is slightly ellipsoidal so damage spot size calculations were made from the measured major and minor axis lengths or by damage area measurements. The following relation was used to calculate an equivalent diameters for ellipsoidal spots with long axis length l_x and short axis of length of l_y:

$$D_{equivalent} = \sqrt{l_x * l_y} \tag{3.6}$$

and equivalent diameters were related to area by this equation:

$$D^2_{equivalent} = 4\frac{A}{\pi} \tag{3.7}$$

3.1.2 Single Pulse Ablation Rate

The depth of material removal per laser shot is important for selection of parameters for scale-up to multi-shot laser machining. The same laser pulse deposition techniques detailed in beginning of this section were used to produce single shot laser spots on samples. The single laser spots were imaged using a DIGITAL INSTRUMENTS Nanoscope IIIa atomic force microscopy (AFM) in tapping mode to characterize the 3D profile of the laser damage. An AFM measurement of a 2.1 J/cm^2 single pulse in 4330 steel is shown in Figure 3.3. A polynomial curve was fit to the raw AFM data to help estimate the average lowest point in the 3D damage profile. A VEECO Laser Profilometer model WYKO NC1100 was also used to determine the depth of material removed by single pulse ablation experiments. The profilometer was operated in the VSI mode allowing for 3 nm resolution in depth at a maximum depth of 2 mm. The laser profilometer collected data at a significantly faster rate with sufficient nanoscaled depth resolution, so this technique was generally used for many later experiments.

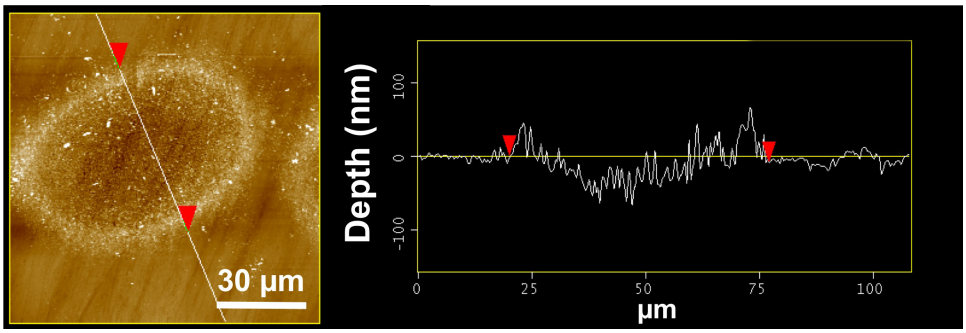

Figure 3.3: (left) AFM scan of single laser pulse in 4330 steel with peak fluence ϕ = 2.1 J/cm^2. A depth of 40 nm is apparent from the line profile on (right). 2D and 3D information is extracted from AFM scans.

3.2 Single Pulse Characterization of 4330 Steel & TiN

Single pulse laser spots were characterized for both 4330 steel and a tool grade TiN coating using the laser profilometer, optical microscopy, and an SEM. The changes in morphology in terms of both the squared-diameter and laser pulse depth have been plotted against laser fluence in Figure 3.4, Figure 3.5, Figure 3.6, Figure 3.7, and Figure 3.8. The ablation thresholds, as calculated using the two-parameter fit for the diameter squared data, for 4330 and TiN were $0.40\,\mathrm{J/cm^2}$ and $0.27\,\mathrm{J/cm^2}$, respectively. In Figure 3.6, the ablation threshold was extrapolated to be significantly lower than for the data collected in Figure 3.4 and Figure 3.5 because the pulse energy data were located much farther from the ablation threshold. The sensitivity of the fit indicated that accurate ablation threshold measurements must be made at low fluences, near the ablation threshold.

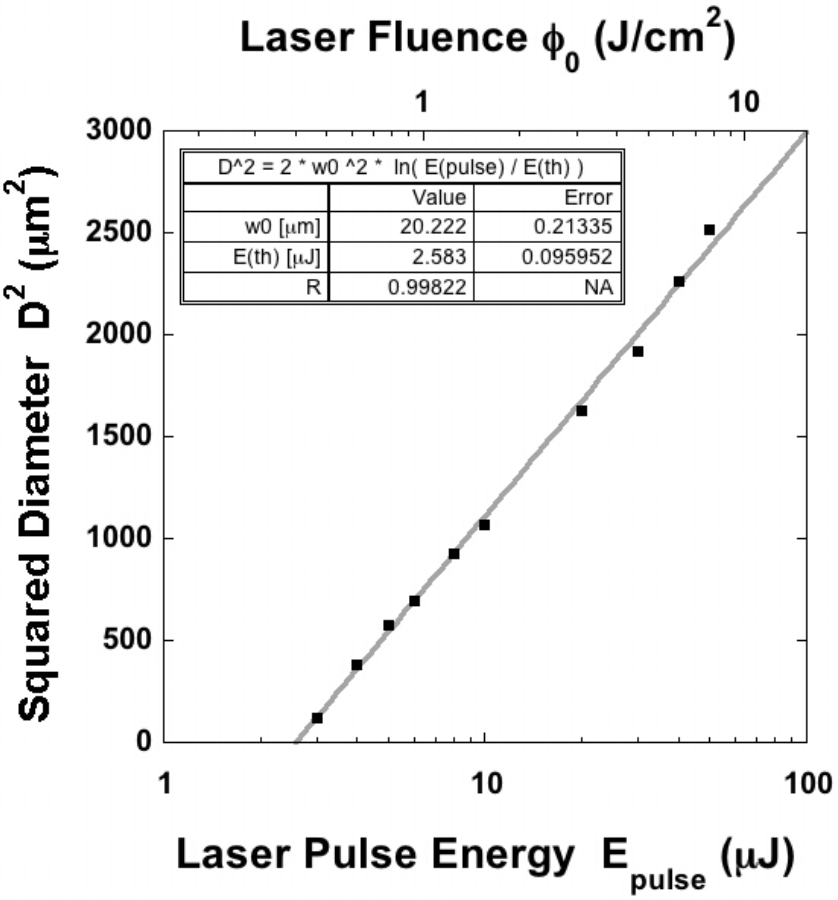

Figure 3.4: Squared diameter of measurements collected from AFM measurements for a 4330 steel irradiated with single laser pulses. An ablation threshold of $0.40\,\mathrm{J/cm^2}$ was extrapolated from the fit of the squared diameter data by pulse energy. The $(1/e^2)$ spot size was calculated from the fit to be 20.2 µm. The $(1/e^2$ spot size is used to determine the laser fluence at the sample surface. The threshold fluence provides a material dependent scale for how much damage is being done to the sample.

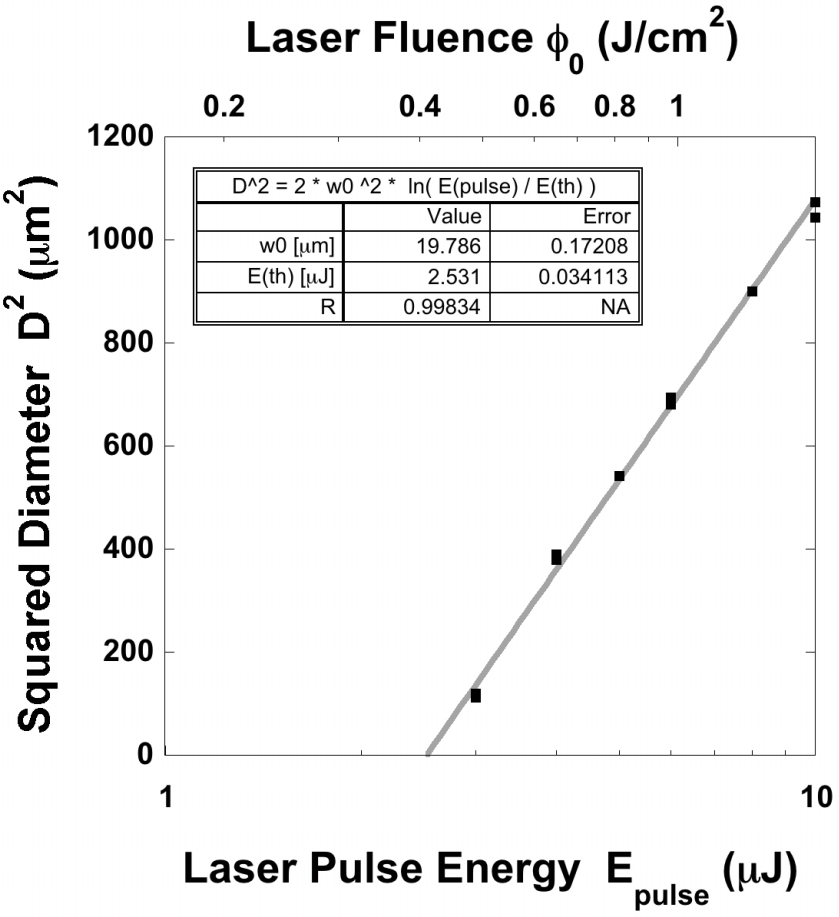

Figure 3.5: Squared diameter measurements collected from AFM measurements for a 4330 steel irradiated with single laser pulses. An ablation threshold of $0.41\,\mathrm{J/cm^2}$ was extrapolated from the fit of the squared diameter data by pulse energy. The $(1/e^2)$ spot size was calculated from the fit to be 19.8 µm. The $(1/e^2$ spot size is used to determine the laser fluence at the sample surface. The threshold fluence provides a material dependent scale for how much damage is being done to the sample.

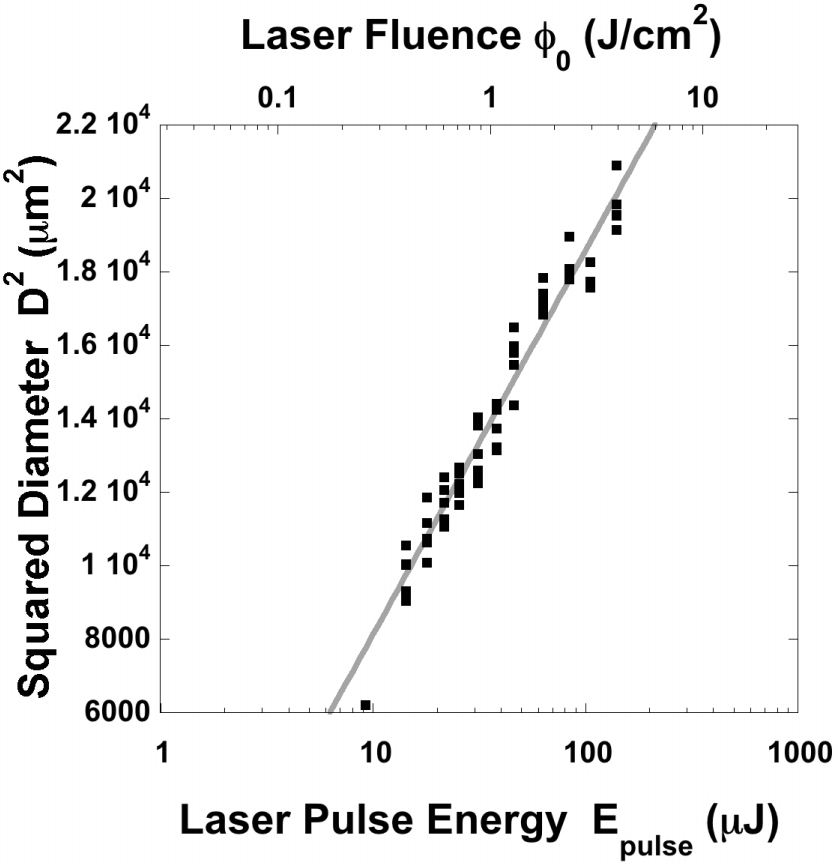

D^2 = 2 * w0 ^2 * ln(E(pulse) / E(th))		
	Value	Error
w0 [μm]	47.623	0.70825
E(th) [μJ]	1.6741	0.16135
R	0.97692	NA

Figure 3.6: Squared diameter measurements collected using an SEM for a 4330 steel irradiated with single laser pulses. An ablation threshold of $0.047\,\mathrm{J/cm^2}$ was extrapolated from the fit of the squared diameter data by pulse energy. The $(1/e^2)$ spot size was calculated from the fit to be 47.6 µm. The $(1/e^2$ spot size is used to determine the laser fluence at the sample surface. The threshold fluence provides a material dependent scale for how much damage is being done to the sample.

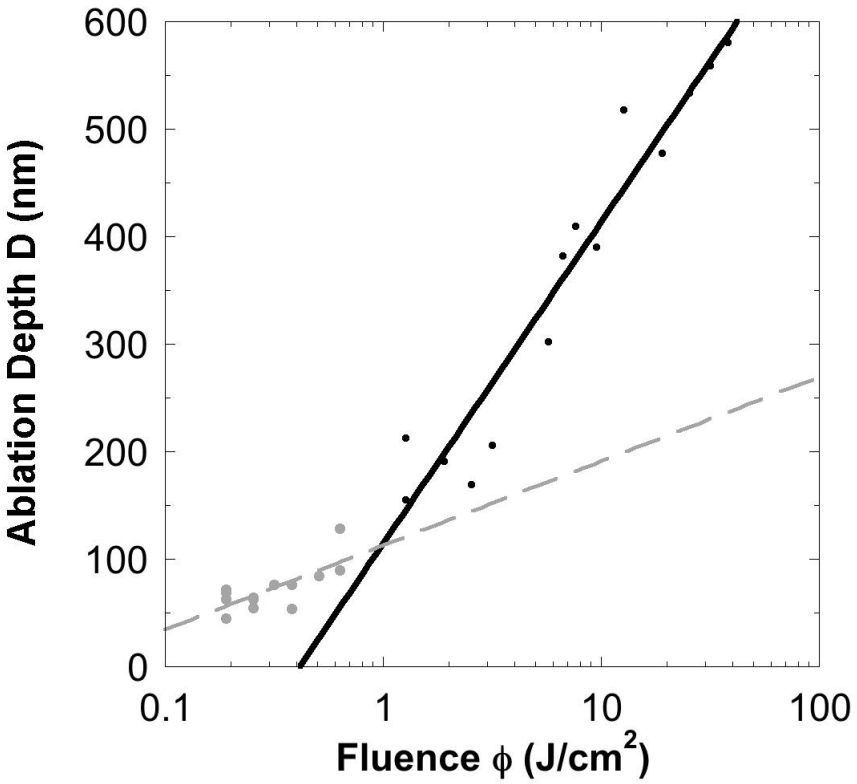

Figure 3.7: Single pulse ablation depths (nm) for 4330 steel plotted against laser fluence (J/cm^2). Ablation depths measured using AFM.

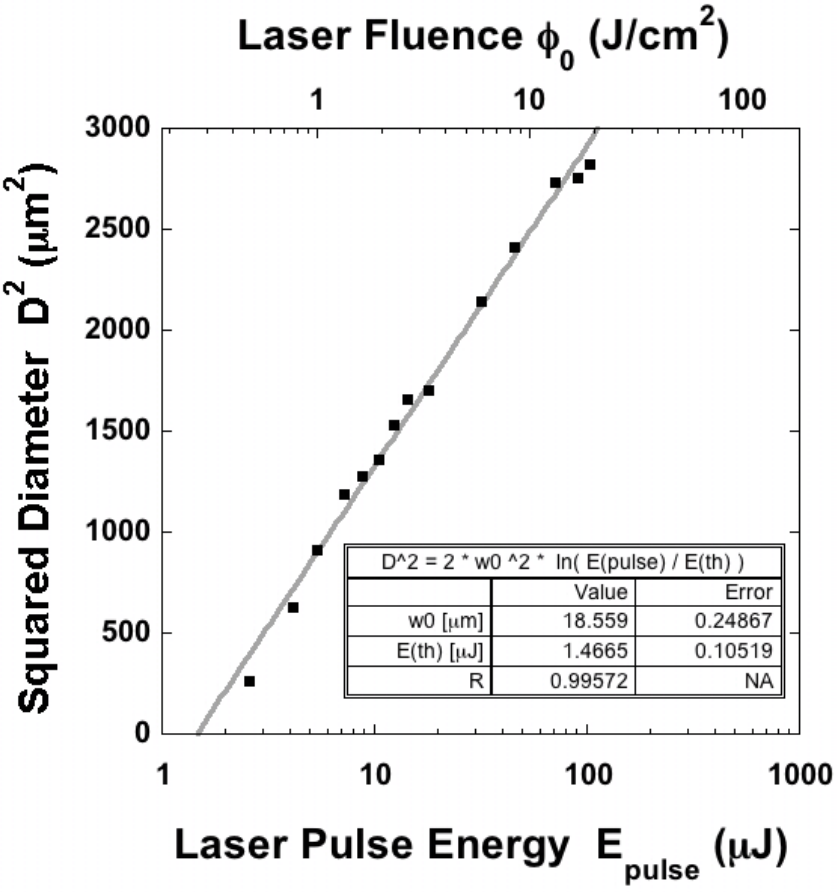

Figure 3.8: Squared diameter measurements collected using an AFM for 4330 steel irradiated with single laser pulses. An ablation threshold of $0.27\,\mathrm{J/cm^2}$ was extrapolated from the fit of the squared diameter data by pulse energy. The $(1/e^2)$ spot size was calculated from the fit to be 18.6 µm. The $(1/e^2$ spot size is used to determine the laser fluence at the sample surface. The threshold fluence provides a material dependent scale for how much damage is being done to the sample.

Many materials are shown to exhibit two different threshold ablation regimes with increasing fluence. In Figure 3.9, a number of fundamentally different materials and their ablation depths are plotted against laser irradiation fluence. All of these materials exhibit two separate ablation regimes, differentiable by a marked change in ablation rate beyond a critical fluence in the range of 0.1-5 $\mathrm{J/cm^2}$.

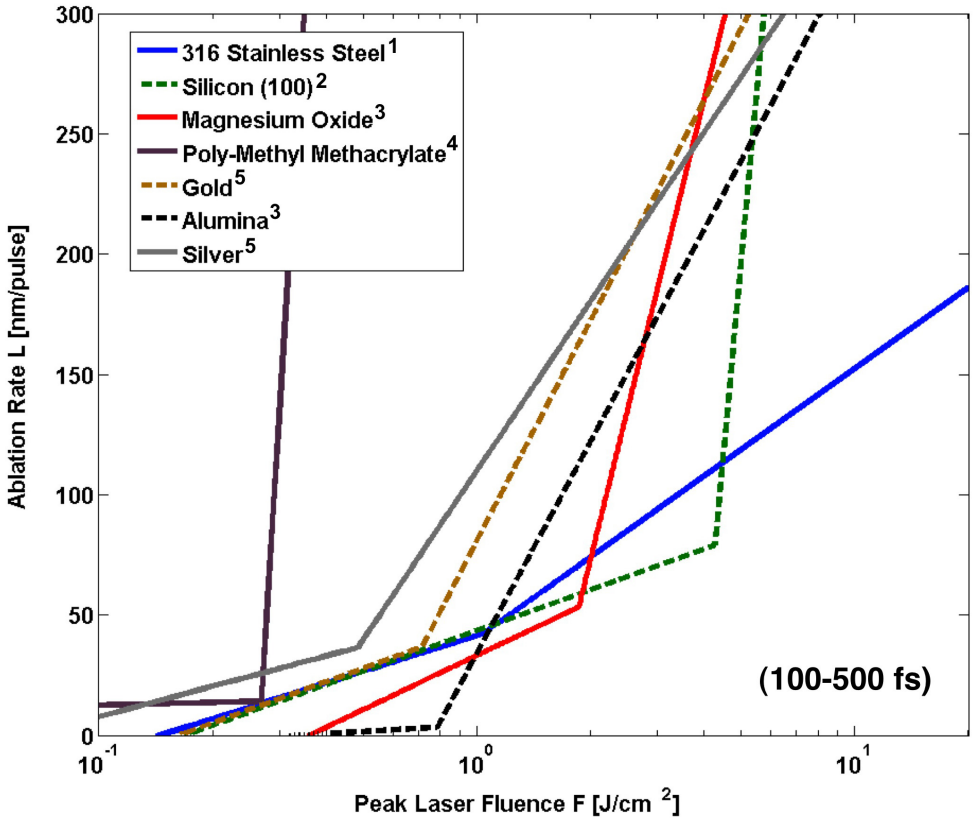

Figure 3.9: Ablation removal rates for 316 stainless steel [119], silicon [100], magnesium oxide [122], poly-methyl-methacrylate [121], gold [123], alumina [122], and silver [123]. All studies were conducted with 100-500 fs. pulses and all curves exhibit a low and high fluence ablation regime with a distinct transition at which the material removal rate sharply increases. This plot shows that materials with multiple phases can be laser machined with simultaneous material removal when their ablation rates are equal. This is only important for multiphase material ablation where the beam has normal incidence to the sample surface.

The 4330 steel samples exhibit the usual two-threshold ablation regimes with distinct thresholds existing at $\phi_{th,1} = 0.19\,\mathrm{J/cm^2}$ and $\phi_{th,2} = 1.0\,\mathrm{J/cm^2}$. Above the $\phi_{th,2}$ threshold laser ablation can produce recast layers with features that appear shock-melted, as appears in Figure 3.10. Between $\phi_{th,1}$ and $\phi_{th,2}$ the material removal produces less surface roughness, particularly near the center of the laser pulse crater, as compared with fluences higher than $\phi_{th,2}$. The decreased roughness in the lower fluence ablation regime also indicates that more consistent material removal will occur.

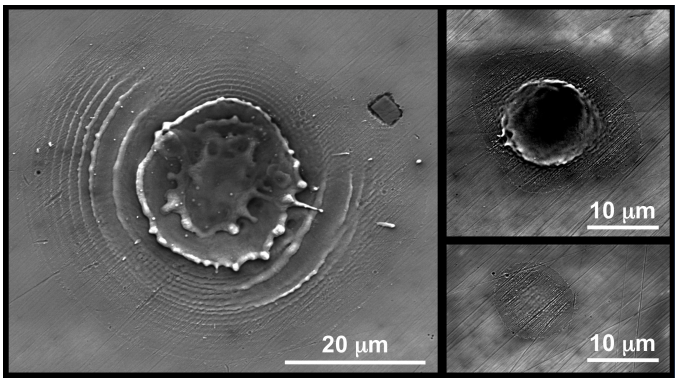

Figure 3.10: Field emission gun (FEG) SEM images of single pulse laser shots on a 4330 steel sample. (left) peak laser fluence ϕ=13.5 J/cm^2 (top right) ϕ=9.6 J/cm^2 (bottom right) ϕ=5.3 J/cm^2.

3.3 Bulk Material Removal

Femtosecond laser irradiation can be focused across a large range of spot sizes, with highly tunable ablation rates. These properties make the laser an excellent tool for tunable material removal. Furthermore, with the laser capable of operating at kilohertz and greater repetition rates, material may be quickly removed from a sample surface with very little collateral damage. Femtosecond lasers have $< 1\%$ pulse-to-pulse power variability permitting the consistent and predictable material removal rates observed in the single pulse experiments.

Since femtosecond lasers are pulsed-type laser systems, bulk material removal has to be performed using aggregated ablation events. For example, a galvometric scanner or a fast moving stage is required to deposit pulses onto separate sample areas without significant pulse-overlap and in a reproducible and controlled manner. Material removal parameters can be described by laser scanning patterns and laser fluence, which will be discussed in more detail in Chapter IV. The laser produces pulses with extremely low power variability (<1 % RMS) and consistent pulse profiles, therefore, the aggregate of many single pulse events will be representative of multi-pulse ablation experiments.

To summarize, the ablation threshold for titanium modified 4330 steel, as measured by SEM, is $0.19\,\mathrm{J/cm^2}$ and the transition from the low to high fluence regimes occurs at $1.0\,\mathrm{J/cm^2}$. When the data from Mannion [119] and Yasumaru [126] is combined, an ideal laser fluence machining range of 0.2-2 $\mathrm{J/cm^2}$ becomes apparent. Therefore, simultaneous two-phase material removal is shown to theoretically exist in the specified laser machining range. In Chapter V, uniform material removal rates are demonstrated experimentally for the TiN containing 4330 steel.

CHAPTER IV

The Femtosecond Laser Based Serial Sectioning Technique

A major component of this research was the development of the femtosecond laser based serial sectioning technique (FSLSS) and the resulting acquisition of 3D datasets using this technique. As such, there were many laser-based experiments performed to develop, calibrate, and validate the FSLSS technique for subsequent application to the TiN containing 4330 steel for acquisition of 3D datasets used in modeling efforts. The material removal rates for laser ablation were calibrated and verified by profilometry and SEM imaging, and then routinely tracked using an automatic focusing routine integrated into the image capture step (see Section 4.3).

The femtosecond laser aided serial sectioning technique has three major components: (1) a focused laser machining station, (2) an optical microscope with a high resolution CCD camera, and (3) a programmable 3-axis stage for sample translation. The serial sectioning procedure is composed of single or multilayer ablation for surface laser machining, followed by a stage translation to the imaging pathway, and then the image acquisition. The equipment used in the sectioning technique will be described in the following chapter.

4.1 FSLSS Components

The CLARK MXR-CPA 2001 femtosecond laser used in these experiments can be highly focused ($> 10^{18}$ W / cm^2) and has ultrashort femtosecond (fs) pulsewidths (150 fs). The wavelength of the coherent radiation produced is 780 nm and operates in a pulsed mode with a repetition rate of 1 kilohertz for the sectioning experiments and 100 Hz for the single pulse experiments. The beam profile is Gaussian and the pulse-to-pulse energy variability is less than 1% RMS with the max pulse energy being $\sim$0.8 mJ. A feedback mode is used during extended machining experiments to maintain the fiber laser pump lamp current, and therefore the laser output power.

The optics setup implemented in the laser machining line includes the following: (1) a polarizer / waveplate combination used to selectively transmit polarized light and thereby controls the average power of the laser, (2) neutral density filters to coarsely attenuate the average beam power, (3) a plano convex lens to bring the beam to the desired machining focal spot size, and (4) a fast acting shutter to regulate laser pulses and machining.

A sample is rigidly affixed to the sample stage to maintain image sampling alignment and stage registration for the machining procedure. Three programmable NEWPORT backlash free ball-screw drive mid-range linear stages are used for sample translations and laser machining. Each stage axis has a resolution of 0.5 µm and unidirectional repeatability of 1.5 µm. The sample is scanned in the laser beam path synchronously with a high speed UNIBLITZ shutter to preferentially deposit laser pulses in the desired region. The laser is oriented so that the laser pulses are delivered orthogonally incident to the sample surface. Forced air is blown parallel to the surface, across the focused laser pulse spots where plasma is being generated, to prevent ablated material from redepositing on the sample surface or the machining optics. This entire FSLSS setup is depicted in Figure 4.1.

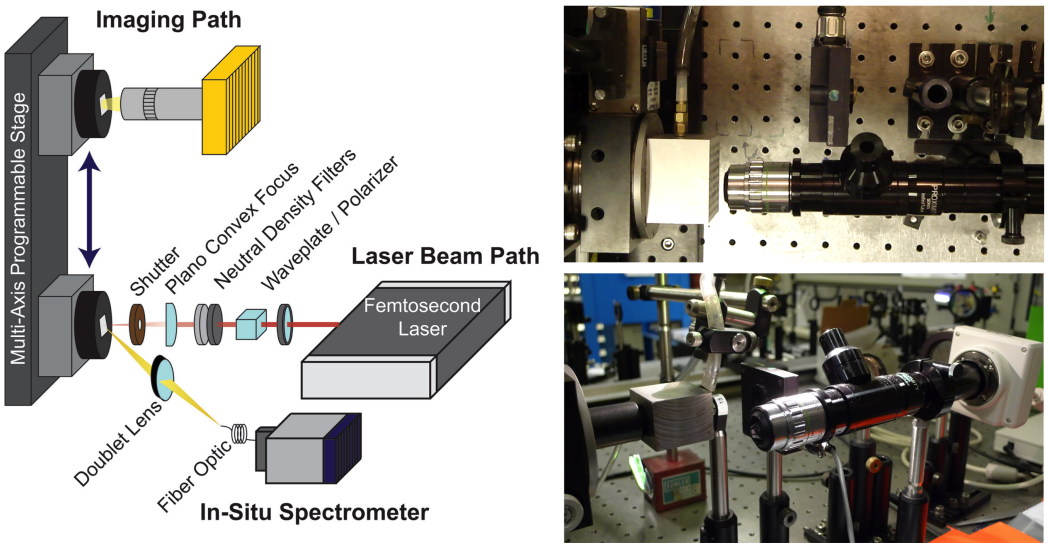

Figure 4.1: (left) Schematic of FSLSS technique. Imaging pathway consists of a microscopy and objective lens coupled to a CCD and images in standard atmosphere. The laser-machining pathway consists of power attenuators and focusing optics. A three-axis stage with the sample rigidly affixed translates the sample and performs the machining steps. An in-situ spectrometer monitors the luminous plasma to capture chemical information. (right) Photographs of schematically shown FSLSS setup.

The currently implemented stage machining pattern and the mechanical laser shutter have been synchronized so that pulses are only deposited on the samples surface once a constant stage velocity criterion has been met. The stage-shutter integration is specifically important for accelerations and decelerations because pulse deposition, and therefore material removal, would not be consistent otherwise. The pattern of motion of the stage is shown in Figure 4.2. The stage is rastered in both of the X and Y stage translating directions, with incremental line spacing motion in the non-rastering direction in between laser scans.

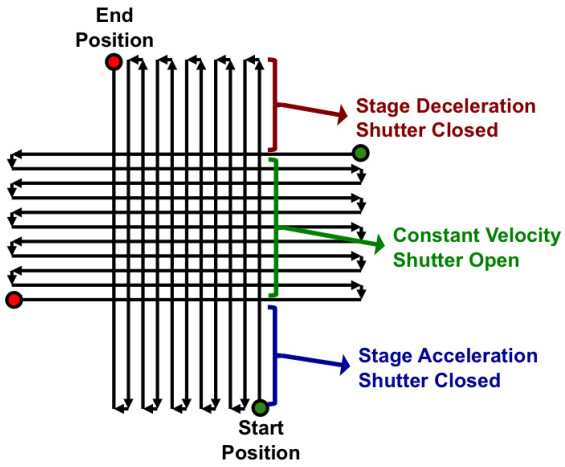

Figure 4.2: Schematic of stage motion for femtosecond laser machining. Accelerations are performed while a fast acting shutter stops the laser pulses. At constant velocities the shutter is opened to laser machine the sample surface. Stage translation is alternated between the horizontal and vertical machining patterns shown overlaid above. The machining patterns are offset by half of the line scan spacing every other iteration to reduce periodic machining artifacts and lower the average surface roughness.

The stage positioning error approaches the microscope objective lens's tolerance in depth of focus. In order to solve this problem, autofocusing software was created; this uses an edge contrast mode or a frequency (Fast Fourier Transform) mode to automatically refocus between the machining and imaging steps. By tracking the difference in the stage position obtained at focus, from slice to slice, the depth of material removed per slice can be measured. The material removal depths are used later, during the 3D reconstruction process to accurately stack the 2D images into 3D space.

The entire FSLSS experiment is controlled using a centralized LABVIEW program that was created to coordinate stage movement, synchronize and actuate shutter closure, capture optical microscope images, autofocus the specimen, translate the stage, and track removal depth. This control process does requires the user to perform basic setup processes, including finding maximum laser focus at the sample surface and calibrating laser fluences. Once setup is complete, the LABVIEW program runs

entirely automated, collecting large datasets unsupervised overnight or on weekends at low-impact laser usage times.

Serial sectioning speeds have been increased with the use of less tightly focusing optics (350 mm to 1000 mm focal length plano-convex lens) and higher average laser power. The same laser fluences are achieved with the use of lenses with a smaller numerical aperture and hence, a larger laser machining spot size. Since the machining pattern used is a rastering method, the speed of the process is linearly related to the speed of the scanning and the line width. Both of these variables are selected based on the ablation spot size, which is a function of the focusing optics. A 1000 mm focal length lens produces a FWHM spot size of 167 µm and an 350 mm focal length lens produced a FWHM spot size of 57 µm. The decrease in line spacing from 45 µm to 15 µm reduces the number of passes per slice by one-third, cutting the machining time in half from 9 to 4 minutes per slice. A slice is defined as any number of sequentially repeated ablation patterns, in this case 4 repeated patterns were made per slice. A scan pattern is illustrated in Figure 4.2.

Currently, the ablation rate for the FSLSS technique is 3.5×10^6 µm^3/min, which is much faster than other types of material removal processes used in serial sectioning techniques such as focused ion beam (FIB) and mechanical polishing. Figure 4.3 compares the material removal rate and maximum sample volume for mechanical polishing, FIB sectioning, and the femtosecond laser. The FSLSS technique can machine large volumes of material because the laser beam is translated using optics and because laser ablation occurs in a non-contact mode. The maximum sample size used in the FSLSS technique depends on the properties of the stage used for translation and not the tool used for material removal. Numerous benefits are gained by decoupling the machining tool from direct physical contact with the sample surface. Benefits include: the precise registration of the stage and the sample, no consumable wear related parts, and consistent beam focus location. After sectioning steps are

performed for a specific material, the sample must have surface quality that permit the imaging of the microstructural component of interest, such as metallic grains and grain boundaries, inclusion phases, dendrite geometry, and porosity. To this end, the femtosecond laser sectioned surfaces have low roughness of $\sim 0.5\,\mu m$. Despite the imparted machining roughness optical images of titanium nitride (TiN) inclusions with sizes of 0.5-1.0 µm and greater have been collected during sectioning experiments of 4330 steel.

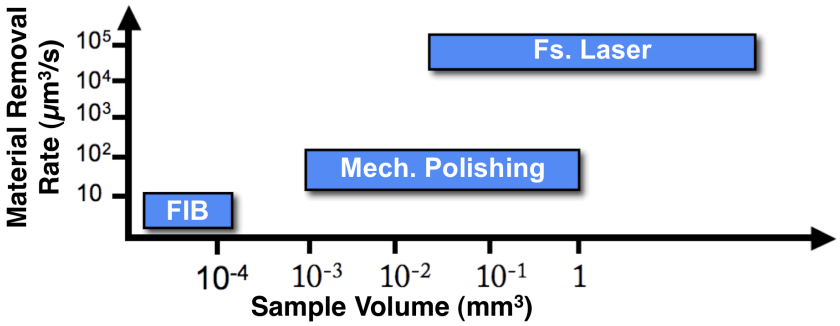

Figure 4.3: Material removal rate plotted against the maximum sectionable volume for mechanical, FIB, and femtosecond laser based serial sectioning techniques.

4.2 Layer-by-Layer Material Removal

Material is removed from a sample surface by either: (1) moving the sample surface under a fixed beam position or (2) scanning the femtosecond laser beam across the sample. In both methods, the laser is scanned with normal incidence to the sample surface. The ablation volume is therefore larger radially, on the incident sample surface, than the depth of material removed. Material ablation is preferable in this alignment because it permits more finely spaced sectioning depths.

The FSLSS technique was originally built to use method (1), fixed beam position with sample translation, which used a Newport mid-range programmable stage to scan the sample under the laser beam. A serpentine scan pattern, shown in Figure 4.2, was designed to work in coordination with a UniBlitz mechanical beam shutter for precise

pulse delivery on the sample surface. The sample is over-scanned before and after the desired ablation area to allow the Newport stage to attain constant linear velocity during pulse deposition. The mechanical shutter is closed for the over-scanned areas, and only opens once the stage is at constant velocity. The sample velocity is linearly related to the pulse spacing as:

$$x_{spacing} = \frac{V_{stage}}{RR_{laser}} \tag{4.1}$$

where $x_{spacing}$ is the center-to-center distance between laser pulses, v_{stage} is the velocity of the stage, and RR_{laser} is the repetition rate of the laser. Now that the location of the center of pulses are known, the spot size of the laser must be determined to calculate the amount of pulse overlap. The spot size of the laser beam can be roughly calculated for a Gaussian beam using the diffraction limited spot size equation, which is:

$$w_0 = 1.27\frac{f}{D}\lambda \tag{4.2}$$

where w_0 is the $1/e^2$ diameter at focus, λ is the wavelength of the coherent light, and $\frac{f}{D}$ is the numerical aperture of the optics being used. Alternately, and often more accurately, a direct measurement of the focused spot size can be made using a CCD camera with high resolution and square pixels or a Beam Profiler. The diameter of the spot size can then be used to calibrate two variables, the line spacing l and the stage velocity v_{stage}. In parametric studies relating the stage velocity v_{stage} and the line spacing l, surface roughness was minimized at 50 % overlap for both variables. Full-width half-max (FWHM) spot sizes for the following optics were measured: for 350 mm focal length lens w_0 was 57 µm and for 1000 mm focal length lens w_0 was 167 µm. Line spacings and stage velocities were proportionately calibrated to the spot sizes based on the 50 % overlap result. Laser machining an area of 1200×1200 µm

with depth ranging from 0.2-0.4 µm, depending on the material, required 4-5 minutes.

The most recent iteration of the FSLSS technique, created earlier this year, has been modified to scan the beam, instead of the sample. Laser scanning is performed using a Newport Fast Steering Mirror (FSM). A gold coated mirror is mounted on a BK-7 glass substrate with electromagnetically driven coils producing digitally encoded mirror deflection. The inertial mass of the FSM laser scanning mirror is at least an order of magnitude less than the mid-range linear stages, which is advantageous for faster scanning speeds and reaching constant velocity. The FSM require a negligible distance to attain constant velocity, resulting in a factor of 10 increase in overall scan speed. A scan area of 750×750 µm with depth ranging from 0.2-0.4 µm, depending on the material, requires less than 30 seconds to laser machine.

4.3 Material Removal Rates

Multi-pulse laser experiments were performed to remove layer-by-layer areas of material. By scanning a laser beam with minimal pulse overlap, high-aspect ratio cubic volumes of material are removed from sample targets. In order to characterize these multi-pulse ablation efficiencies, techniques needed to be developed to track material removal via the laser. Initial calibrations for the bulk material removal rates were made using measurements with a stylus-profilometer. Once the precise removal rates were established, an integrated auto-focus based depth profiling routine was used to track material removal in-situ.

4.3.1 Profilometry

Profilometry was used to experimentally measure the depth in multi-shot laser machined areas. These areas were prepared using the same ablation pattern shown for the serial sectioning experiments, shown in Figure 4.2. The multi-shot areas were machined with a focused laser spot size of 57 µm with 50 % overlapping line and pulse

spacing. A collective 580 laser passes, or 145 slices with 4 passes per slice, were used to laser machine a square area of 1.5×1.5 mm with depth of 37.5 µm or ∼65 nm/pass. The depth of these deeply machined areas was measured using a contacting-mode DEKTAK 3 profilometry stylus and the data is shown in Figure 4.4. The depth was measured by performing a line-trace measurement across the un-machined sample and into the machined area, to determine the step size. The profilometry data and the average roughness of both the machined and un-machined areas were obtained. Bulk laser pulse removal rates were calculated by dividing the total depth removed by the total number of pulses deposited onto a fixed area. The current post machining average roughness (Ra) has been measured to be between 0.1-0.4 µm for low ablation-regime laser fluences in 4330 steel (see Figure 4.5).

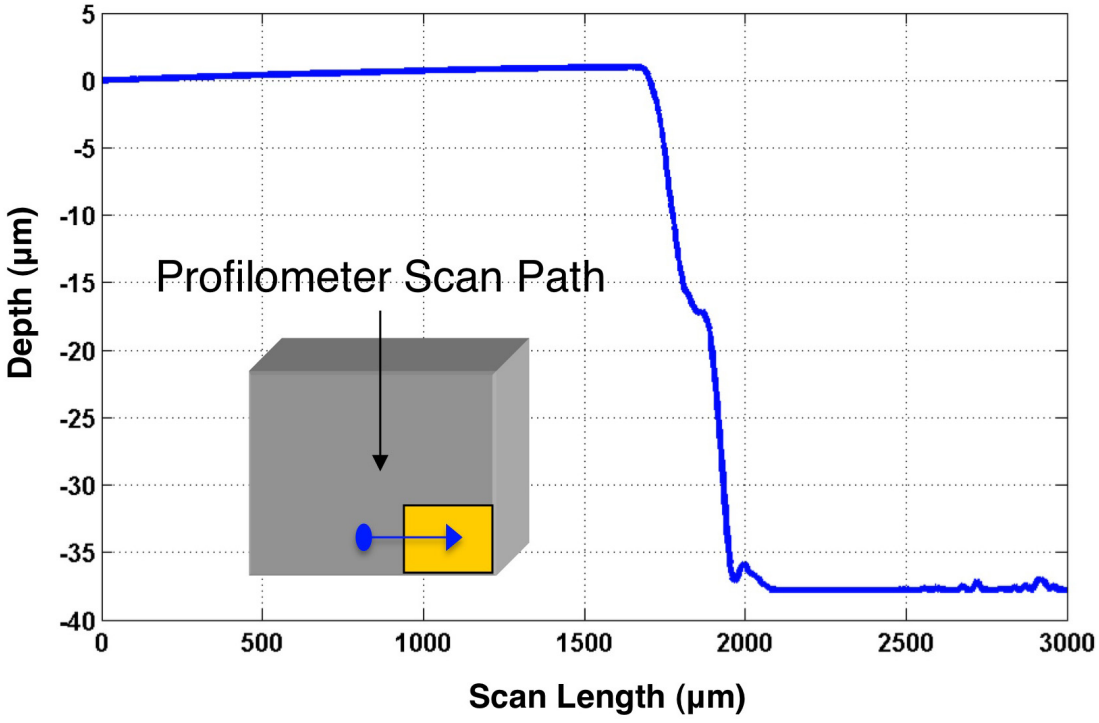

Figure 4.4: Schematic and plot of data collected using a profilometer to characterize the step height for repeated square area laser ablation scans. The step size is 37.5 µm which was removed over the aggregate of 580 laser passes or about 64.7 nm/pass. Pulse overlap was less than 20%.

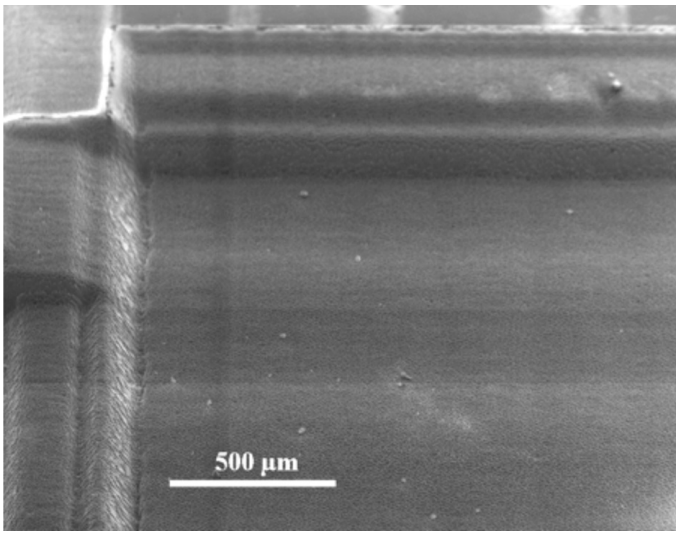

Figure 4.5: SEM image of 4330 steel after 80 µm of material removal using the FSLSS technique. Sample surface has an average roughness (Ra) of 0.5 µm.

4.3.2 Autofocus Depth Profiling

In order to measure the laser ablation depths in situ, an optical microscope was coupled to three-axis programmable NEWPORT mid-range travel linear stages. Multi-pulse laser ablation was performed in one position, and then imaging was performed in a secondary translated stage position. A MITUTOYO 20x imaging objective coupled to a INFINITUBE in-line lighting microscope was used to collect optical micrographs of the laser ablated sample surface. As material was removed in a serial process, one layer at a time between imaging steps, the sample surface falls out of the focal plane compared to the previously imaged position. Therefore, an autofocus routine was incorporated into automated stage control to bring the sample back into focus between machining steps. By tracking the change in stage position necessary to maintain peak optical focus, the material removal rate is also directly measured. The Rayleigh range of the 20x objective is $\sim$0.6 µm providing adequate sub-micron resolution for depth tracking. The material removal rate is linear, Figure 4.6, allowing for an average removal rate to be calculated from the average change in stage positions

over the course of a multi-layer laser material removal experiment.

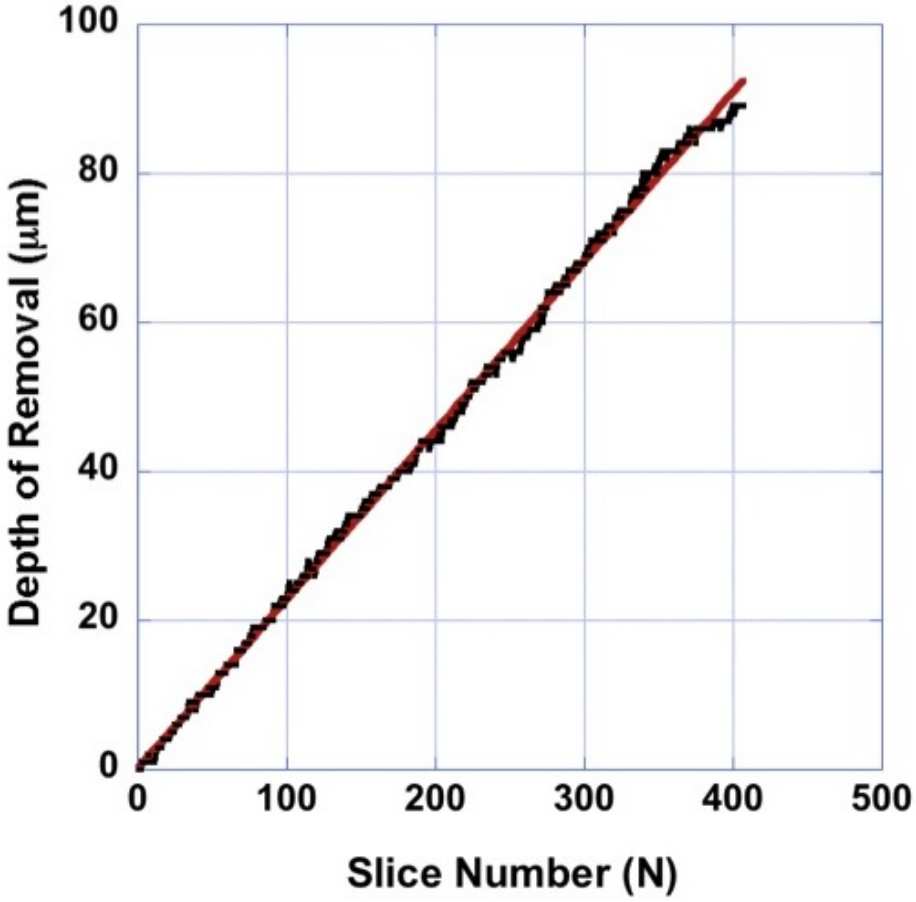

Figure 4.6: The material removal, as determined by an autofocusing routine, is linear throughout the entire sectioning experiment (41 hours). The sample surface is brought into focus using a Fast-Fourier-Transform algorithm to provide open loop feedback for small stage movements. The stage position, at focus, is recorded for every slice and then plotted to determine the material removal rate.

4.4 Image Acquisition

Between each machining step (slice), the sample is imaged using a microscope objective lens coupled with a 5.0 megapixel CCD sensor. The LABVIEW control program operates an integrated autofocus routine, which ensures that the sample surface is at optimal focus; it also has the capability to acquire images at multi-

ple stage positions for stitching and reconstruction of larger, high resolution areas. Using the autofocus data from the calculated average removal rate an overall material removal summary can be reconstructed. Imaging resolution is dependent upon the magnification of objective lens used to resolve the image and the CCD sensor size and resolution. With a 20x objective the in-plane resolution for this setup is $\sim 0.15\,\mu m$/pixel and with a 50x objective the in-plane resolution is $\sim 0.07\,\mu m$/pixel.

4.5 Image Segmentation Routines

Image segmentation is the process by which microstructural interfaces are identified and segregated using image processing tools. Discerning interfaces of most microstructural features is fairly straightforward for humans, but computers have immense difficulty being programmed to recognize the same details and pattern recognition. The image processing routines used to segment the raw FSLSS image data have evolved during the course of the project. Preliminary routines consisted of adjusting contrast, simple filtering, and standard thresholding routines. More advanced manual methods were coded that consist of a series of 3D region growing [127] steps manually seeded with human input for the microstructural feature locations. The identified and segmented individual particles were then compiled into a complete dataset. Currently, fully automated MATLAB segmentation routines, developed in collaboration with N. Husseini (University of Michigan: Applied Physics), perform all the image processing steps and output binary-segmented images. Many different automated routines have been designed to segment the various types of microstructures being interrogated. The automated code developed for segmentation of inclusion particles in steel consists of a series of steps summarized here: a background average calculated for the entire dataset, background average subtraction for the entire raw data stack, identification of peak intensity pixel values, threshold filter radiating outward radially from peak intensified values, a disk smoothing routine, and removal of single

pixel erroneous detections. The fully automated segmentation process only requires a run time of about 30 seconds per image. In Figure 4.7 some of the segmentation steps are shown for a raw optical image of 4330 steel from a FSLSS dataset. Image registration, which is the alignment of slices in the stack, was not necessary due to the sub-micron resolution of the 3-axis Newport stage.

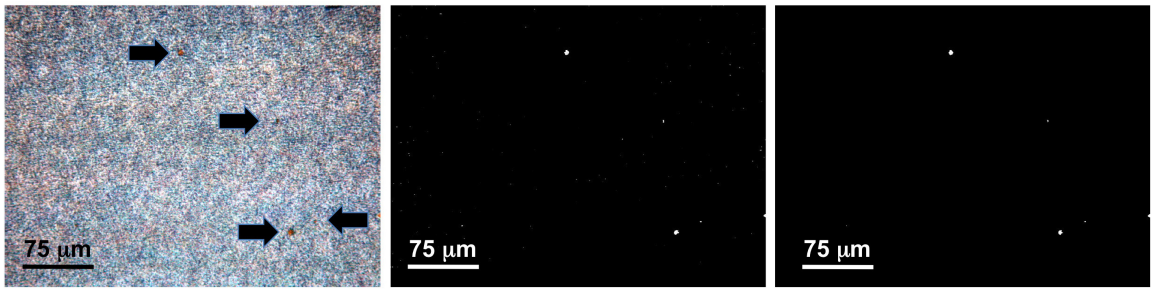

Figure 4.7: (left) Raw optical image from FSLSS process with TiN inclusion particles identified with arrows. (middle) Same image after background subtraction and a local threshold being applied to the highest R/G/B color intensity ratio areas. (right) Same image in final segmented form with a disk filter smoothing routine and deletion of single pixel point detections with no nearest neighbors (26 total) in any plane.

4.6 Reconstruction Methods

Visualization of the segmented 3D images occurs in a three-step process. Currently, we use IDL visualization code developed by D. Rowenhorst (NRL) and the open source PARAVIEW software. First, the images are loaded into memory and then stacked into a 3D voxelized array - see Figure 4.8. A polygon surface mesh is fit to the voxelized array, which can be input directly into the IDL visualization code or into PARAVIEW. The 3D statistical analysis of the inclusion particles was performed using IDL code from H. Jou (QUESTEK LLC: Evanston, IL). To calibrate the visualizations correctly, the resolution and voxel sizes must be defined. For the imaging plane (X and Y axis), the CCD resolution is used for the voxel spacing. In the sectioning direction (Z axis), the material removal rate from the auto-focusing routine is used to define the voxel spacing. Typically the imaging plane resolution

is higher than the sectioning resolution due to the inherent coarseness of sectioning. The FSLSS method produced nearly square voxels because of the precise machining control of multi-pulse laser ablation.

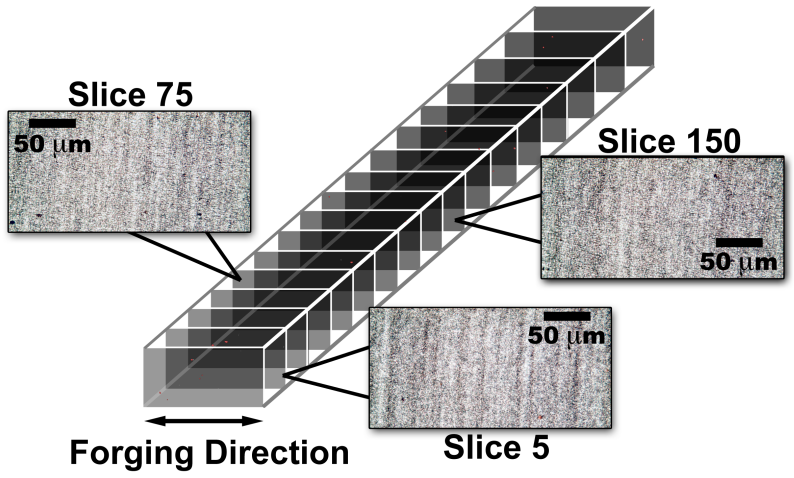

Figure 4.8: Raw optical FSLSS images expanded from a schematic 2D segmented image stack. The images are assembled with a spacing equal to the material removal rate calculated for the specific FSLSS experiment.

4.7 Ablation Artifacts

During the process of calibrating the laser fluences necessary to remove multiple phases simultaneously, many ablation artifacts have been discovered. These artifacts tend to be coupled with either the scanning parameters or the laser focusing conditions. Surface quality can be defined as a combination of surface roughness and periodic surface texturing. Generally, surface modification is visible on three length scales. These are, (1) sub-micron sized polarization induced ripples, (2) non-uniform multi-phase ablation artifacts, and (3) $> 5\,\mu m$ scanning parameter related artifacts.

Laser polarization produces sub-micron scaled features known as ripples, shown in Figure 4.9. These ripples have fine scaled roughness visible in multi-pulse laser machining experiments and have been demonstrated in the literature on numerous

occasions [102, 128]. They are commonly produced in laser processing of materials, such as metals, semiconductors, and dielectrics, for lasers having a periodic wavelength ranging through most of the visible spectrum and for continuous pulse lasers down to ultrashort pulsed lasers [129]. The rippling has been shown to have a spacing on the order of the wavelength of the laser light [130, 131], and in the case of a titanium:sapphire femtosecond laser, 780 nm.

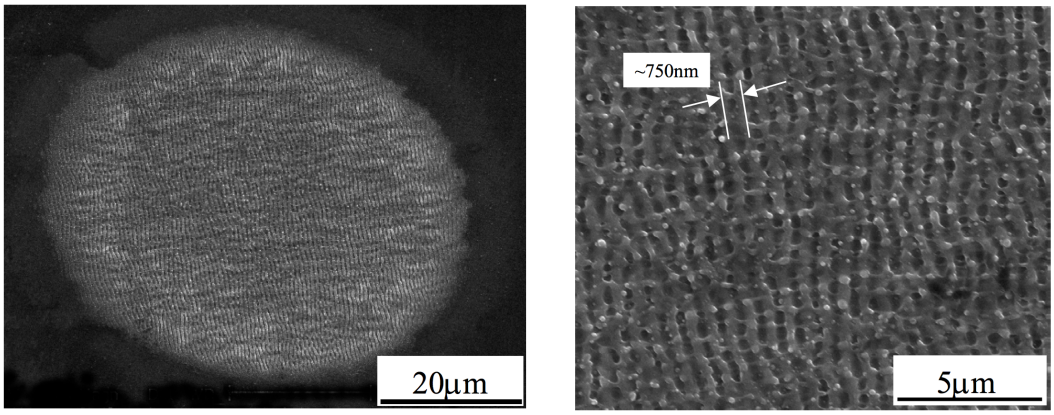

Figure 4.9: Secondary electron SEM image of 16 laser pulses at $0.54\,\mathrm{J/cm^2}$ on a single-crystal nickel based superalloy CMSX-4 [88]. Small ripple formations are shown to form at a length scale similar to that of the laser radiation (780 nm). The ripples are oriented parallel to the polarization of the laser wavefront. (left) low magnification. (right) high magnification

In multiphase materials, preferential ablation can create local topology during a sectioning experiment. Preferential phase ablation can occur when ablation rates are not matched in laser ablation with normal incidence to the sample surface (see Figure 3.9). For instance, small mounds may form between a matrix material with a faster removal rate and an inclusion phase with a slower removal rate, shown in Figure 4.10 - bottom left. The differential laser removal rate is exacerbated by the complex geometries that form between the two phases. In Figure 4.10 - bottom right, a large peak has formed. Once a peak forms between two phases, it often will persist or grow, with continued laser scanning, because of the non-planar interface formed between the fast and slow ablating phases. Reduced laser ablation rates can occur

when laser pulses are distributed over a larger area because of the steep or near vertical interfaces that form between phases and the associated change in laser absorption and reflection. Intermediate scale roughness can develop due to non-uniform ablation of separate phase regions, in the case of TiN particles in 4330 steel, the particles and the artifacts are spaced ranging from 5-25 µm. This occurs when a phase is preferentially etched, creating a plateau or peak where the phase with the slower ablation rate resides. A peak that is formed in this manner often forms a preferentially sharper aspect ratio, due to the larger area over which pulses are deposited (steeper angle - larger area of deposition) and reduced beam absorption resulting from the sharper aspect ratio. A peak and some second-phase particles ablating at rates different from the matrix are shown in Figure 4.10 - top right and bottom left.

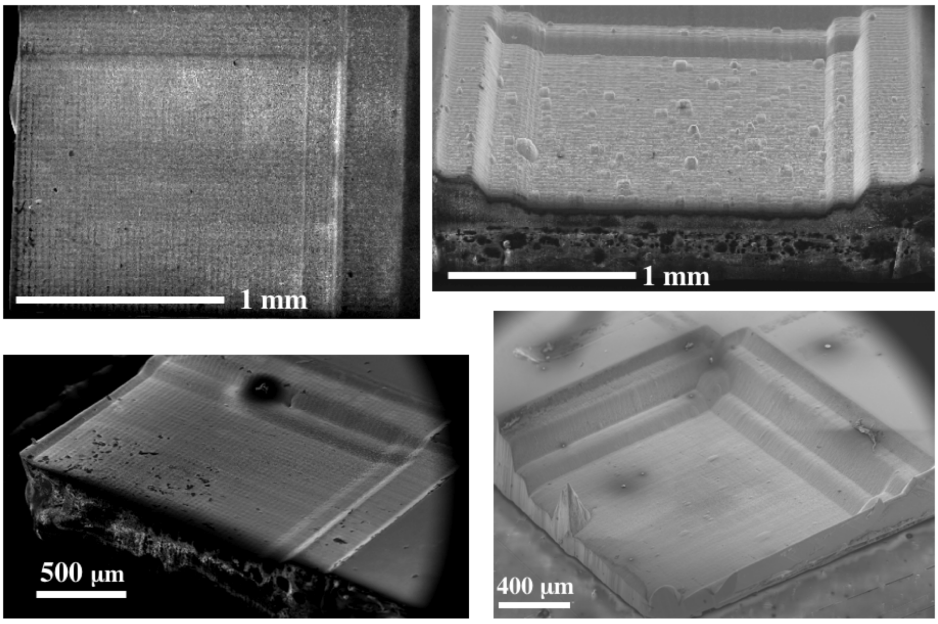

Figure 4.10: (top left) Laser machining of lanthanum oxide containing steel. The laser ablation scan paths are visible from line spacing that was larger than 50 % overlap. (top right) Mounds formed from nonuniform ablation of second phase lanthanum oxide precipitates in steel. (bottom left) Laser scan lines are visible and lanthanum oxide phases that have been exposed by sectioning. (bottom right) A peak has formed presumably from non-matched ablation of two phases, again in a lanthanum oxide containing steel.

If scanning protocols are not optimized for the focused beam spot size, surface

texturing develops on the order of the line spacing or the pulse size. By overlapping pulses more by reducing the scan-line spacing and by introducing a dithered shift in the ablation pattern, periodic structures on the order of 10-50 µm are removed. Large scale periodic structures are visible in Figure 4.11 where a scan line spacing of $\sim 10\,\mu m$ was chosen for a $1/e^2$ spot size of 18 µm. Laser scan parameters can create periodic structures that are dependent on the scan line spacing or the pulse-to-pulse spacing in the scan direction. In Figure 4.12, scan lines are visible in the ablated area. Clearly, the line spacing was configured to be too large, with little pulse overlap - as is evident by the periodic topology. In Figure 4.13, a schematic is shown depicting the compounding laser scan line problems. In the FSLSS technique, a shift of the ablation pattern by one-half of the line spacing was introduced to reduce the effective line spacing by a factor of 2. Inherent stage positioner errors are beneficial in reducing roughness by preventing line scans to occur along exactly the same paths for every slice. The laser repetition rate is not synchronized with the stage scanning, which introduces randomized pulse deposition, in the direction of travel. Therefore, the likelihood of pulses falling in exactly the same location along the scan paths for two different laser scans would be very low.

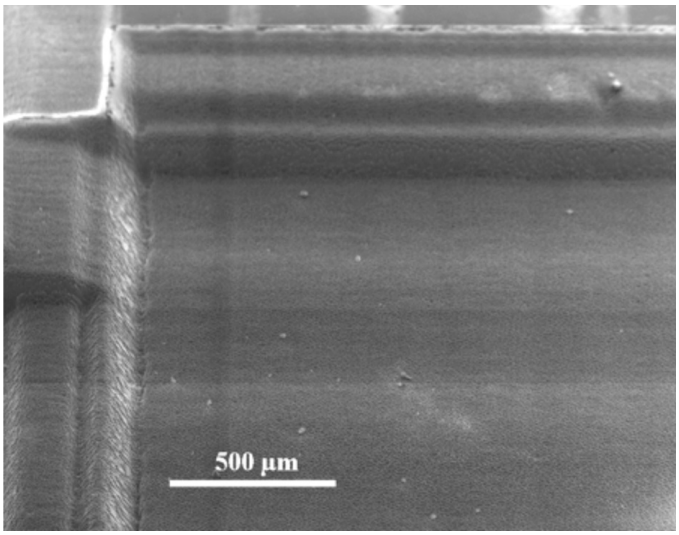

Figure 4.11: Secondary electron SEM image of polycrystalline nickel with periodic machining artifacts due to non-optimized line spacing. The width of the artifacts is 9.2 µm, which was approximately equal to the scan line spacing.

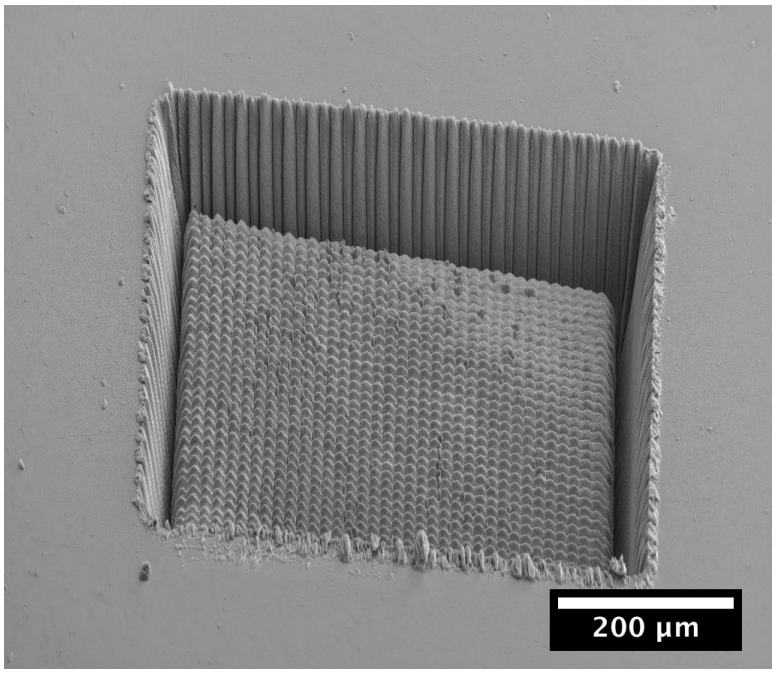

Figure 4.12: SEM image of polycrystalline nickel after 200 µm of material removal using the FSLSS technique in vacuum. Periodic structures have formed as a result of the 9.3 µm line spacing.

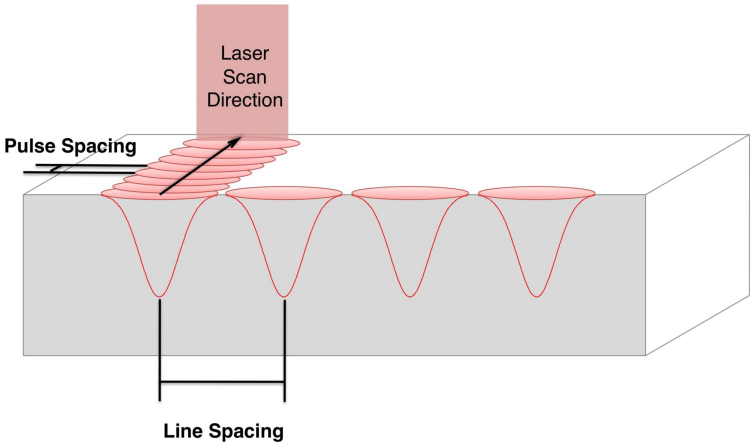

Figure 4.13: A schematic showing the line spacing, pulse spacing, and Gaussian beam profile. Periodic machining artifacts will occur if these parameters are not optimized.

Laser ablation artifacts are detrimental to laser machining during the FSLSS technique, because planar areas of material must be uniformly removed in order for the 3D reconstructions to be representative of the actual microstructure. The artifacts could be useful for other applications though. An example of this is shown in Figure C.1 and Figure C.2, where an alumina fiber reinforced magnesium alloy has been preferentially etched by laser ablation. The images on the (left), in both Figure C.1 and Figure C.2, have been machined with a few passes of the ablation pattern, whereas the images on the (right) have been scanned hundreds of times. In these optical microscope images, the matrix is out of focus after intensive laser machining, because it has been removed at a greater rate than the alumina fibers that still remain visible.